A Multiwavelength View of the Rapidly Evolving SN 2018ivc: An Analog of SN IIb 1993J but Powered Primarily by Circumstellar Interaction

Keiichi Maeda[1] , Poonam Chandra[2] , Takashi J. Moriya[3,4] , Andrea Reguitti[5,6,7] , Stuart Ryder[8,9] , Tomoki Matsuoka[1] ,
Tomonari Michiyama[3,10] , Giuliano Pignata[5,6] , Daichi Hiramatsu[11,12,13,14] , K. Azalee Bostroem[15] , Esha Kundu[16,17] ,
Hanindyo Kuncarayakti[18,19] , Melina C. Bersten[20,21,22] , David Pooley[23] , Shiu-Hang Lee[1] , Daniel Patnaude[24] ,
Ósmar Rodríguez[25] , and Gaston Folatelli[20,21,22]

[1] Department of Astronomy, Kyoto University, Kitashirakawa-Oiwake-cho, Sakyo-ku, Kyoto, 606-8502. Japan; keiichi.maeda@kusastro.kyoto-u.ac.jp
[2] National Radio Astronomy Observatory, 520 Edgemont Road, Charlottesville, VA 22903, USA
[3] National Astronomical Observatory of Japan, 2-21-1 Osawa, Mitaka, Tokyo 181-8588, Japan
[4] School of Physics and Astronomy, Faculty of Science, Monash University, Clayton, Victoria 3800, Australia
[5] Instituto de Astrofísica, Universidad Andres Bello, Fernandez Concha 700, Las Condes, Santiago, Chile
[6] Millennium Institute of Astrophysics (MAS), Nuncio Monsenor Sótero Sanz 100, Providencia, Santiago, Chile
[7] INAF—Osservatorio Astronomico di Padova, Vicolo dell'Osservatorio 5, I-35122 Padova, Italy
[8] School of Mathematical and Physical Sciences, Macquarie University, NSW 2109, Australia
[9] Macquarie University Research Centre for Astronomy, Astrophysics & Astrophotonics, Sydney, NSW 2109, Australia
[10] Department of Earth and Space Science, Osaka University, 1-1 Machikaneyama, Toyonaka, Osaka 560-0043, Japan
[11] Center for Astrophysics | Harvard & Smithsonian, 60 Garden Street, Cambridge, MA 02138-1516, USA
[12] The NSF AI Institute for Artificial Intelligence and Fundamental Interactions, USA
[13] Las Cumbres Observatory, 6740 Cortona Drive, Suite 102, Goleta, CA 93117-5575, USA
[14] Department of Physics, University of California, Santa Barbara, CA 93106-9530, USA
[15] DiRAC Fellow, DiRAC Institute and Department of Astronomy, University of Washington, 3910 15th Avenue NE, Seattle, WA 98195-0002, USA
[16] International Centre for Radio Astronomy Research, Curtin University, Bentley, WA 6102, Australia
[17] Center for Data Intensive and Time Domain Astronomy, Department of Physics and Astronomy, Michigan State University, East Lansing, MI 48824, USA
[18] Tuorla Observatory, Department of Physics and Astronomy, FI-20014 University of Turku, Finland
[19] Finnish Centre for Astronomy with ESO (FINCA), FI-20014 University of Turku, Finland
[20] Instituto de Astrofísica de La Plata (IALP), CONICET, Argentina
[21] Facultad de Ciencias Astronómicas y Geofísicas, Universidad Nacional de La Plata, Paseo del Bosque, B1900FWA, La Plata, Argentina
[22] Kavli Institute for the Physics and Mathematics of the Universe (WPI), The University of Tokyo, Institutes for Advanced Study, The University of Tokyo, 5-1-5
Kashiwanoha, Kashiwa, Chiba 277-8583, Japan
[23] Department of Physics and Astronomy, Trinity University, San Antonio, TX, USA
[24] Smithsonian Astrophysical Observatory, Cambridge, MA 02138, USA
[25] The School of Physics and Astronomy, Tel Aviv University, Tel Aviv 69978, Israel

Abstract

SN 2018ivc is an unusual Type II supernova (SN II). It is a variant of SNe IIL, which might represent a transitional case between SNe IIP with a massive H-rich envelope and SNe IIb with only a small amount of the H-rich envelope. However, SN 2018ivc shows an optical light-curve evolution more complicated than that of canonical SNe IIL. In this paper, we present the results of prompt follow-up observations of SN 2018ivc with the Atacama Large Millimeter/submillimeter Array. Its synchrotron emission is similar to that of SN IIb 1993J, suggesting that it is intrinsically an SN IIb–like explosion of an He star with a modest ($\sim$0.5–1$M_\odot$) extended H-rich envelope. Its radio, optical, and X-ray light curves are explained primarily by the interaction between the SN ejecta and the circumstellar material (CSM); we thus suggest that it is a rare example (and the first involving the "canonical" SN IIb ejecta) for which the multiwavelength emission is powered mainly by the SN–CSM interaction. The inner CSM density, reflecting the progenitor activity in the final decade, is comparable to that of SN IIb 2013cu, which shows a flash spectral feature. The outer CSM density, and therefore the mass-loss rate in the final $\sim$200 yr, is higher than that of SN 1993J by a factor of $\sim$5. We suggest that SN 2018ivc represents a missing link between SNe IIP and SNe IIb/Ib/Ic in the binary evolution scenario.

1. Introduction

Core collapse supernovae (CCSNe) are explosions of massive stars at the end of their evolution (e.g., Langer 2012). CCSNe provide an unparalleled opportunity to study the yet to be clarified evolution of massive stars in their final phase. In the

standard picture, the observational classification of CCSNe is assumed to be associated with the nature of the progenitor stars (Filippenko 1997). SNe IIP, showing H lines and an optical light-curve plateau, are the explosion of a red supergiant (RSG) with zero-age main-sequence (ZAMS) mass in the range of $M_{\rm ZAMS} \sim 8$–$18M_\odot$ (Smartt 2009), likely dominated by those with $M_{\rm ZAMS} \lesssim 12M_\odot$ for a well-observed sample (Martinez et al. 2022).

SNe Ib show He lines but not H lines, while SNe Ic show neither H nor He lines; they are believed to be the explosion of a compact He or C+O star (Langer 2012). SNe IIb represent a

transitional case between SNe IIP and Ib, and their progenitors are thought to be an He star with a smaller amount of the H-rich envelope left at the time of the explosion compared to that of SNe IIP (Nomoto et al. 1993; Woosley et al. 1994; Bersten et al. 2012; Bufano et al. 2014). SNe IIb/Ib/Ic are collectively called stripped-envelope SNe (SESNe), since they form a sequence of the envelope stripping during the evolution toward the SN explosion. The progenitor mass range for SESNe is not as clear as that for SNe IIP; it has been suggested by some that most SESNe share the same (or similar) mass range of SNe IIP (Lyman et al. 2016; Taddia et al. 2018), but others (Anderson et al. 2012; Groh et al. 2013; Smartt 2015; Kuncarayakti et al. 2018) have argued otherwise. Binary interaction is also suggested as the main driver for the H-rich envelope stripping that creates the transition from SNe IIP to these "classical" SESNe (Yoon 2017; Fang et al. 2019; Sun et al. 2022).

Besides SNe IIP, there are other subclasses that belong to SNe II. SNe IIL are characterized by a linear decline in their light curves (e.g., Barbon et al. 1979), while sharing the dominance of H lines with SNe IIP. The profiles of H lines in SNe IIL are characterized by a strong emission component, with a blueshifted absorption component shallower than those seen in SNe IIP (Gutiérrez et al. 2014). While SNe IIP and IIL were originally divided into two distinct populations (Arcavi et al. 2012), the increasing sample now suggests that they lie on a continuous sequence (Anderson et al. 2014). The lack of a plateau suggests that the progenitors of SNe IIL contain a smaller amount of the H-rich envelope than those of SNe IIP, which might then place SNe IIL as a transitional class between SNe IIP and SNe IIb (Moriya et al. 2016; Hiramatsu et al. 2021). As an alternative scenario, the main difference between SNe IIP and IIL could be attributed to a dense circumstellar material (CSM) in the vicinity of the progenitor (Morozova et al. 2017). These scenarios do not necessarily require that the progenitors of SNe IIL share the same initial mass range of those of SNe IIP (and SESNe); the exact nature of the SN IIL progenitors (e.g., the ZAMS mass and the mechanism for the H-rich envelope stripping) remains unclear.

Recent developments in both high-cadence surveys and rapid follow-up observations have led to the discovery of various types of transients that do not fit into the classical classification scheme. The unusual SN II 2018ivc is one such example (Bostroem et al. 2020). SN 2018ivc was discovered soon after the explosion and then intensively followed up with various telescopes, leading to a uniquely comprehensive data set from the very infant phase. While its optical spectra are overall similar to those of SNe IIL, the optical light curves of SN 2018ivc show more complicated behavior than those of canonical SNe IIL (Figure 1; Bostroem et al. 2020). They showed an initial peak in absolute magnitude of $r \sim -17$ mag and a rapid decay in the first 1 week, then a short plateau at ~ -16.5 mag up to ~ 20 days. After the plateau, the magnitude dropped by ~ 1 mag in about 1 week, which was then followed by a linear decay at a rate in the range found for SNe IIL. From the frequent changes in the decay slope, together with the X-ray detection and the boxy profiles in optical emission lines, Bostroem et al. (2020) suggested the presence of an interaction between SN ejecta and CSM.

Radio emission from SNe serves as a unique tool to probe the nature of the CSM, as this signal is essentially powered by the SN–CSM interaction alone (e.g., Chevalier 1998; Björnsson & Fransson 2004; Chevalier & Fransson 2006;
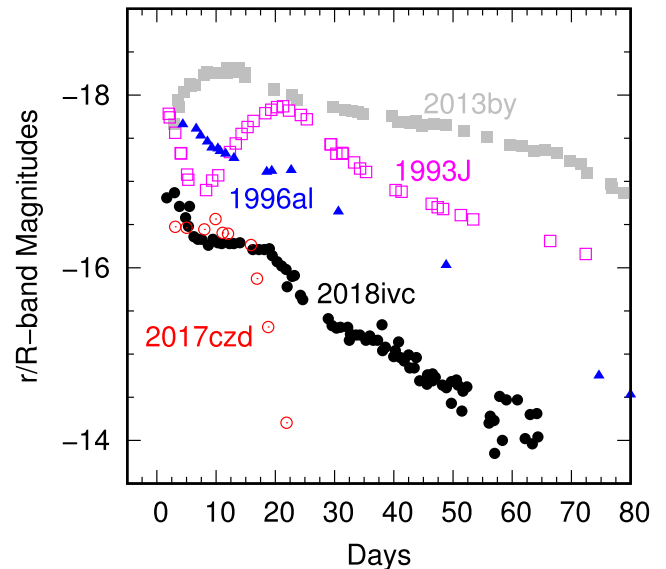

Figure 1. Comparison of the (absolute-magnitude) r/R-band light curves of SN 2018ivc and some selected objects. Shown here are SN IIL 2013by (Valenti et al. 2015), peculiar SN IIL 1996al (Benetti et al. 2016), SN IIb 1993J (Richmond et al. 1994), and faint SN IIb 2017czd (Nakaoka et al. 2019).

Matsuoka et al. 2019). In this paper, we present our target-of-opportunity (ToO) follow-up observations of SN 2018ivc with the Atacama Large Millimeter/submillimeter Array (ALMA). Thanks to the rapid communication of the early discovery and quick classification, we were able to observe SN 2018ivc with ALMA from ~ 3 days after the discovery. Covering a phase up to ~ 200 days, the data allow us to constrain the nature of the CSM around SN 2018ivc from the immediate vicinity of the progenitor ($\lesssim 10^{15}$ cm) to outer regions ($\gtrsim 10^{16}$ cm). The present analysis thus allows us to unravel the progenitor evolution of SN 2018ivc and its relation to other types of CCSNe.

The paper is structured as follows. In Section 2, we present the ALMA observations and data reduction. We then investigate the nature of the ejecta and the CSM based on the ALMA data in Section 3. This is further quantified with a synchrotron emission model in Section 4. The same model is then applied to the optical and X-ray emission in Section 5, where we conclude that the emission at various wavelengths is mainly powered by a single mechanism, i.e., the SN–CSM interaction. Based on the properties of the SN ejecta and the CSM, we discuss the progenitor evolution of SN 2018ivc in Section 6; we suggest that this is a transitional object between SNe IIP and IIb that has been predicted in the binary evolution scenario. We conclude in Section 7 with a summary of our findings.

2. Observations and Data Reduction

SN 2018ivc was discovered by the $D < 40$ Mpc SN survey (DLT40; Tartaglia et al. 2018) on 2018 November 24 UT and the discovery was publicly reported almost in real time (Valenti et al. 2018). Its infant nature was immediately noticed by a deep last-nondetection image from DLT40 on 2018 November 19, and subsequent rapid follow-up observations (Bostroem et al. 2020). Its spectral classification as a young SN II was reported within a day of the discovery (Yamanaka 2018; Zhang et al. 2018). It occurred 8″7 east and 16″1 north of the center of the Seyfert galaxy NGC 1068 (M77). Despite its low redshift

Table 1
ALMA Measurements of SN 2018ivc

MJD	Phase (days)	F_ν (with 1σ Error) (mJy)	On-source Exposure (minutes)	Array	Resolution
Band 3 (100 GHz)					
58,449.10	4.1	4.25 ± 0.22	5.0	C43-4	$0.\!''71 \times 0.\!''69$
58,452.11	7.1	7.42 ± 0.38	5.0	C43-4	$1.\!''16 \times 0.\!''71$
58,462.11	17.1	9.05 ± 0.46	5.0	C43-4	$1.\!''29 \times 1.\!''04$
58,643.62	198.6	0.336 ± 0.026	19.7	C43-9	$0.\!''064 \times 0.\!''047$
Band 6 (250 GHz)					
58,449.10	4.1	4.21 ± 0.43	10.6	C43-4	$0.\!''30 \times 0.\!''27$
58,451.17	6.2	4.32 ± 0.44	10.6	C43-4	$0.\!''48 \times 0.\!''35$
58,462.13	17.1	2.49 ± 0.28	10.6	C43-4	$0.\!''53 \times 0.\!''47$
58,643.58	198.6	0.120 ± 0.022	41.8	C43-9	$0.\!''029 \times 0.\!''018$

Note. The phase was measured from the putative explosion date MJD 58,445.0 (A. Reguitti et al. 2022, in preparation).

($z = 0.0038$), the distance has a relatively large uncertainty. We adopt $10.1^{+1.8}_{-1.5}$ Mpc based on the Tully–Fisher method (Tully et al. 2009), as also used by Bostroem et al. (2020) and A. Reguitti et al. (2022, in preparation).

Immediately after the classification report, we activated ToO observations of SN 2018ivc with ALMA through the Cycle 6 program 2018.1.01193.T (PI: K. Maeda), which was designed to target a young CCSN soon after explosion. The data were taken at three epochs starting on 2018 November 27 UT, spanning a range of $\sim$4–17 days after the putative explosion date (MJD 58,445.0; A. Reguitti et al. 2022, in preparation).[26] Additionally, we observed SN 2018ivc at a late phase ($\sim$200 days) through the Director's Discretionary Time (DDT) program 2018.A.00038.S (PI: K. Maeda). A log of the ALMA observations is shown in Table 1. We used band 3 (with central frequency 100 GHz) and band 6 (250 GHz) at each epoch. The spectral windows (SPWs) were composed of four single continuum windows, centered at 93, 95, 105, and 107 GHz for band 3 and at 241, 243, 257, and 259 GHz for band 6, with a bandwidth of 2 GHz each, avoiding the wavelengths of potentially strong molecular bands. The same spectral setup was adopted in all the epochs. The array was in the C43-4 configuration (resulting in an angular resolution of $\sim$1″ in band 3 and $\sim$0.″5 in band 6) for the first three epochs, while it was in the C43-9 configuration ($\sim$0.″05 in band 3 and $\sim$0.″025 in band 6) at the last epoch. Thanks to the higher angular resolution and the longer exposure, the last-epoch observation provides much higher sensitivity than the first three epochs. We note that the case of SN 2018ivc highlights the power of ALMA's combination of high sensitivity and high angular resolution; the relatively close proximity of the SN position to the radio-bright core of a Seyfert galaxy makes ALMA virtually the only instrument able to robustly detect this SN at millimeter wavelengths.

The data were calibrated through the standard ALMA pipeline with CASA version 5.4.0-70, in a manner similar to that adopted for SN Ic 2020oi by Maeda et al. (2021). We measured the flux densities using the CASA *imfit* task. The final error in the flux density measurements for the combined continuum windows includes the error in *imfit*, the image rms, and the uncertainty in the flux calibration. The flux densities are reported in Table 1, and the reconstructed images are shown in

Figure 2. The spectral energy distributions (SEDs) at the four epochs and the light curves are shown in Figures 3 and 4, respectively.

SN 2018ivc is clearly seen to be an evolving point source with ALMA. The high spatial resolution in the final epoch corresponds to $\sim$2.5 pc (band 3) or $\sim$1.3 pc (band 6) at the distance of NGC 1068. The maximum recoverable scale in the final epoch ($\sim$0.″8 in band 3) corresponds to $\sim$40 pc, comparable to the beam size in the first three epochs. We do not see any strong sources within this region other than the SN, confirming that any contamination from the unresolved background in those images would be negligible.

3. Properties of Radio Emission from SN 2018ivc

3.1. Observational Features

Figure 3 shows that the SED peak is between 100 and 250 GHz on day 4, indicating that the emission is optically thin at 250 GHz from the beginning. The peak moves toward lower frequency as time goes by, probably passing through band 3 (100 GHz) at around day 7. By day 17 the SED peak has moved well below 100 GHz, and the emission between 100 and 250 GHz becomes entirely optically thin; the spectral slope between 100 and 250 GHz on day 17 is consistent with that expected for optically thin emission in the cooling regime ($f_\nu \propto \nu^\alpha t^\beta$ and $\alpha \sim -1.5$). By day 199, the SED slope has changed to $\alpha = -1.12 \pm 0.22$ (1σ), consistent with the adiabatic regime frequently observed for radio SNe (see Section 3.2 for details). While SN 2018ivc's being fully in the cooling regime at this time is rejected at the $\sim 2\sigma$ level, the SN may still experience a moderate cooling effect.

Thanks to the high signal-to-noise detections, the spectral slope within each band can be discerned from the individual SPWs, except for band 6 (250 GHz) on day 199. At 250 GHz, the decrease toward higher frequency is seen from the beginning, confirming that the emission has been optically thin at 250 GHz across the entire period of the ALMA observations. At 100 GHz on the other hand, we see a transition from optically thick to optically thin emission, with an increase toward higher frequency on day 4, a flattening by day 7, and then a decrease with frequency by day 17. We conclude that the emission is in the optically thin regime between 17 and 199 days at 100 GHz, and between 4 and 199 days at 250 GHz. The temporal slope in the optically thin regime provides strong diagnostics on the underlying physical

---

[26] This is consistent with the estimate by Bostroem et al. (2020) of MJD 58,444.25 $\pm$ 1.8.
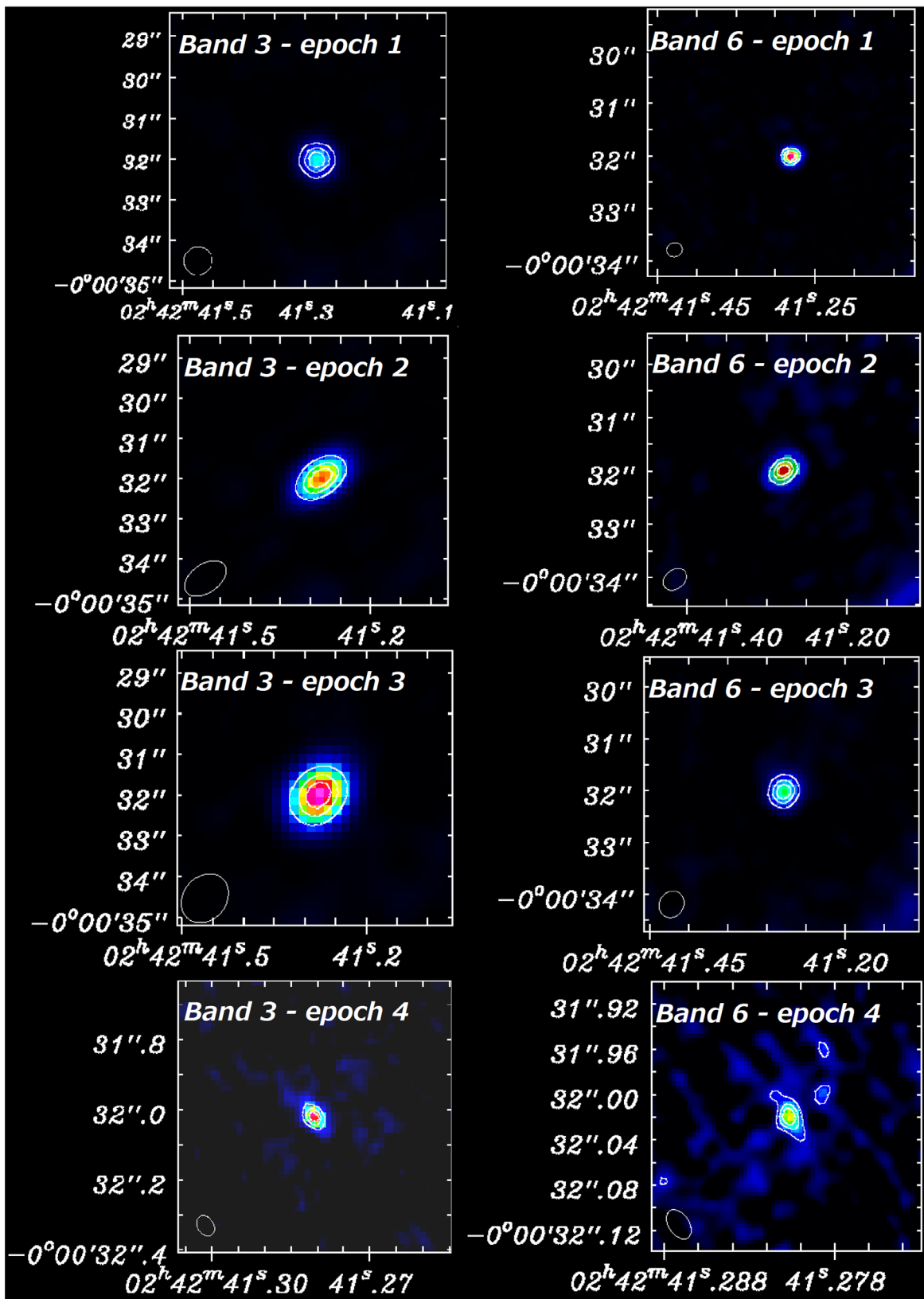
Figure 2. The ALMA band 3 (left column) and band 6 (right column) images of SN 2018ivc, at four epochs (from top to bottom; see Table 1). In the images for the first three epochs, the color is normalized by the flux density range [0:10 mJy] for the band 3 images and by [0:5 mJy] for the band 6 images. At the last epoch, the ranges are [0:0.4 mJy] for band 3 and [0:0.2 mJy] for band 6. The contours represent 35%, 60%, and 80% of the peak flux density. The elliptical beam shape is shown on the bottom left corner in each panel. The angular scale shown here is similar for the first three epochs, while it is much smaller in the last one with a long-baseline configuration.
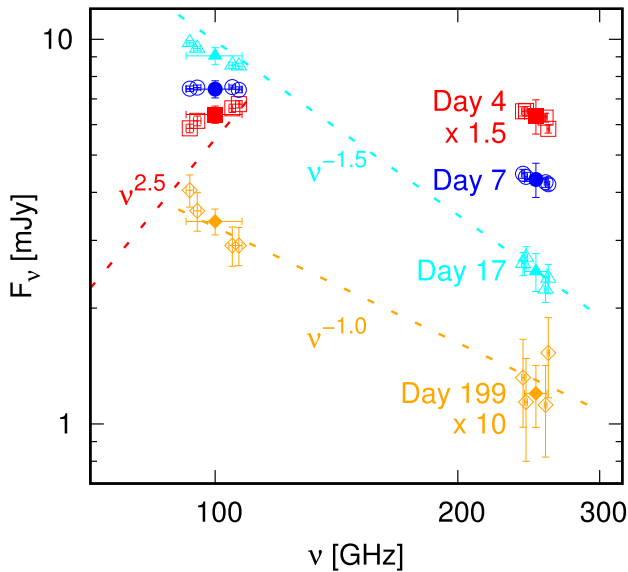
Figure 3. The SEDs of SN 2018ivc on days ∼4 (red squares), 7 (blue circles), 17 (cyan triangles), and 199 (orange diamonds). The flux densities derived for the individual SPWs are shown by open symbols, while the flux densities after combining the four continuum SPWs within each band are shown by filled symbols. The flux densities are shown with 1σ error bars; the flux calibration uncertainty is included for the SPW-combined data, but omitted for the individual SPW data. For demonstration purposes, the expected spectral slopes are shown for the optically thick regime ($F_\nu \propto \nu^{2.5}$; to compare them with the data on day 4), and for the optically thin regime with strong cooling effect ($\propto \nu^{-1.5}$; on day 17) and with negligible cooling effect ($\propto \nu^{-1}$; on day 199).

Figure 4. The high-frequency radio light curves of SN 2018ivc, constructed from the ALMA data at 100 GHz (red open squares) and 250 GHz (blue filled squares). The flux densities are shown with 1σ error. For demonstration purposes, the flux evolution in the decay (optically thin) phase is connected by dashed lines with the power-law indices indicated by the labels. Also plotted here for comparison is the (optical–NIR) bolometric light curve (black open circles), for which the flux (y-axis) is arbitrarily scaled.

conditions (e.g., Maeda et al. 2021); it is basically determined by the SN ejecta density and CSM density distributions, supplemented by the energy distribution of accelerated electrons and cooling processes as detailed in Section 3.2.

The late-time light-curve evolution after day 17 (Figure 4) can be fit with a decay rate $\beta = -1.35$ at 100 GHz and -1.24 at 250 GHz. A decay rate of -1.35 is typical of late-time optically thin synchrotron emission seen for SESNe (Chevalier & Fransson 2006). While the difference is only at the ∼1σ level, the slightly flatter decay at 250 GHz may indicate the importance of a cooling process at least in the early phase (Section 3.3). We note that the lack of any data between days 17 and 199 makes it possible that the light curves have a more complicated behavior, e.g., a combination of initially flatter and then steeper evolution, than the smooth behavior assumed here. However the single-slope evolution is similar to that typical of SESNe, and is similar to the behavior of the optical light curves (Bostroem et al. 2020) (Figure 4 and Section 5). Thus we believe a single-power-law decay in the late phase is most likely the case, and our main conclusions would not be affected since we are tracing the mean behavior in the late phase in our subsequent analyses.

The earlier evolution is not as simple however. Between days 7 and 17, we can safely assume that the emission is optically thin at 250 GHz (see above). The temporal slope here is different from that in the later phase; it is much flatter with $\beta \sim -0.54$. While the increasing importance of the cooling effect can make the light curve flatter in the earlier phase (Björnsson & Fransson 2004; Maeda 2013a), this effect alone would not explain the large change in the temporal slope, as explained in Section 3.3. We note that a similar evolution, with a steepening around day 20, is seen in the optical light curve (Bostroem et al. 2020) (Figure 4). This indicates that the
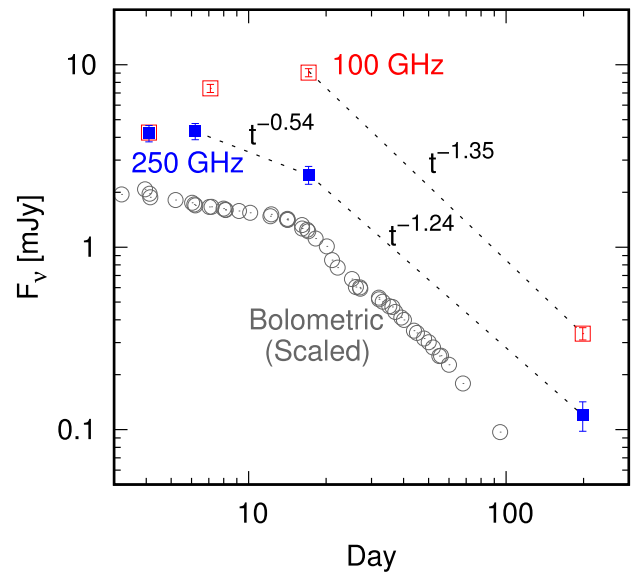
change in the temporal slope is driven by a mechanism shared by both the radio and optical emission. This leads to the possibility that the optical emission could also be mainly powered by the SN–CSM interaction, and there might be a change in the CSM properties probed by the shock wave around day 20. We will present emission models in Sections 4 (radio) and 5 (optical and X-ray) showing that the characteristics of the temporal evolution in the radio emission provide a strong constraint on the CSM structure.

3.2. General Constraints on Properties of the Ejecta and the CSM Density

The most frequently used diagnostic in studying radio emission from SNe is the relation between the peak luminosity and the time taken to reach that peak (Chevalier 1998; Chevalier & Fransson 2006). Under several standard assumptions, it is independent of the observing frequency if the peak epoch is appropriately scaled (i.e., $t_{\rm p} \propto \nu^{-1}$, where $t_{\rm p}$ is the observed time to peak at frequency ν). Since the radio emission from SNe is most frequently observed at ∼5 GHz, this frequency is usually adopted for the scaling.

From this relation one can draw lines along which the shock velocity is constant (Chevalier 1998), or along which the same ejecta properties (i.e., a combination of the ejecta mass ($M_{\rm ej}$) and the kinetic energy ($E_{\rm K}$)) are expected (Maeda 2013a). Along such lines, a denser CSM results in a slower and more luminous peak emission. While the exact relation between the theoretical lines and the actual ejecta/CSM properties suffers from uncertainties in the microphysical parameters for the synchrotron emission, the peak relation nevertheless provides a good estimate for the properties of the ejecta and the CSM separately once the relation is calibrated by a "template" SN for which these properties have been robustly derived by other methods. For example, the ejecta properties of SN 1993J have
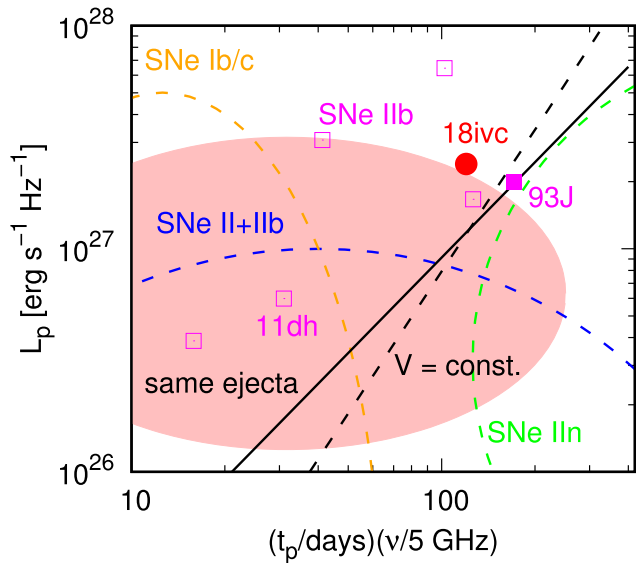
Figure 5. The relation between peak epoch and peak luminosity for various SN types. The distribution of each subtype (Bietenholz et al. 2021) at the 68% confidence level is shown for SNe IIb (filled pink region), SNe Ib/c (orange dashed line), SNe IIn (green dashed line), and a combination of SNe II and IIb (blue dashed line). Some SNe IIb (Soderberg et al. 2012) are shown with magenta squares (the filled symbol is for SN 1993J). Under the standard model framework with a simple CSM structure, the relation for a constant shock velocity of 10,000 km s^{-1} is shown by the black dashed line, and that for a given combination of ejecta properties (M_{ej} and E_K) is shown by the black solid line. The position of SN 2018ivc (filled red circle) in this diagram comes from a model light curve at 5 GHz, extracted from the late-time ALMA light curves (Model A, Section 4).

been estimated to be $M_{ej} \sim 3$–$3.5 M_\odot$ and $E_K \sim 1$–1.2×10^{51} erg (Shigeyama et al. 1994) through the optical light curve and spectra, and thus SNe having similar ejecta properties will lie roughly along the solid line marked in Figure 5 in their peak radio properties. Furthermore, CCSNe of different subtypes appear roughly separated in this peak luminosity/epoch relation (Chevalier & Fransson 2006), albeit with some overlaps (Bietenholz et al. 2021). SNe IIP are generally fainter than SESNe, and SNe IIn are slower and brighter than SESNe. SESNe are distributed above the line for a shock velocity of $\sim 10,000$ km s^{-1}, while SNe IIP are mostly below this line.

In reality several assumptions in the above description may not be valid, such that the relation between the peak time and the peak luminosity could be dependent on the observing frequency. Since our observations are at 100 and 250 GHz, the CSM we probe with our data is indeed at a much smaller scale than that probed at 5 GHz for the same object; for example, given that the peak time roughly follows $t_p \propto \nu^{-1}$ (as expected from a simple model with a smooth CSM distribution), the peak time is earlier by a factor of ~ 20–50 at these high frequencies, and therefore the physical scale of the CSM we are probing is smaller by the same factor (which is indeed one of the motivations for such high-frequency observations; Matsuoka et al. 2019; Maeda et al. 2021). There is no guarantee that the CSM distribution can be described by a single power law at such differing scales; indeed, we will soon show that this is not the case. In addition, the effect of the cooling is more substantial for these higher frequencies, and this results in a difference from the simple standard picture that assumes synchrotron emission in the adiabatic regime.

For all these reasons, simply using the light curves at 100 GHz or at 250 GHz would not provide a fair comparison to

other SNe. Therefore, we use instead a model for the synchrotron emission that explains the light curves at 100 and 250 GHz in the late phases ($\gtrsim 17$ days; Section 4), and extract the predicted 5 GHz light curve from this model. The estimate on the peak date and luminosity for SN 2018ivc is shown in Figure 5. The fact that the peak date at 5 GHz thus derived falls within the periods covered by our observations gives us some confidence in this approach.

We find that the peak properties of SN 2018ivc are similar to those of SNe IIb, and separate from those of SNe Ib/c and SNe IIP/L. In particular, the similarity to the prototypical SN IIb 1993J in peak radio properties (van Dyk et al. 1994; Fransson & Björnsson 1998) is striking. The positions of both SN 1993J and SN 2018ivc in Figure 5 are unique for SNe IIb and suffer little from overlaps with other subtypes.[27]

The peak properties thus indicate that the ejecta properties of SN 2018ivc are similar to those of SNe IIb, and that the CSM properties are also overall similar to those of SN 1993J. We however emphasize that this is a somewhat qualitative argument. For example, it is not guaranteed that the microphysical parameters for the synchrotron emission are universal for different SNe, and so further quantifying this conclusion and identifying differences from SN 1993J will require a more detailed comparison between the observed data and a radio synchrotron emission model (Section 4), with an effort to provide additional constraints through independent arguments (e.g., multiwavelength modeling; Section 5).

3.3. General Constraints on the Distribution of the CSM

The analysis of the peak behavior has shown that the properties of the CSM around SN 2018ivc are overall similar to those of SN 1993J. Further insight can be obtained by studying the temporal evolution (see, e.g., Maeda 2013a; Maeda et al. 2021).

The late-time light-curve evolution after day 17 is relatively simple and in line with the expectation from the standard SN–CSM interaction scenario. As mentioned in Section 3.1, the decay rate of $\beta \sim -1.35$ is typical of late-time optically thin synchrotron emission from SESNe. Describing the synchrotron characteristics by $f_\nu \propto \nu^\alpha t^\beta$, the spectral slope ($\alpha$) is dependent only on the power-law index (p) in the distribution of the relativistic electrons as a function of the energy, assuming it is described by a single power law. From Figure 3, $p \sim 3$ is robustly derived (following $\alpha = -p/2$ in the cooling regime; see below), and we adopt this value throughout the present work. We note that this value is typical for SESNe (Chevalier & Fransson 2006; Maeda 2013b). The temporal slope (β) is then determined by the CSM density distribution ($\rho_{CSM} \propto r^{-s}$) and the shock wave expansion dynamics ($R \propto t^m$). The expansion rate of the shock wave (m) is indeed determined by the combination of the CSM distribution slope (s) and the outer density distribution of the SN ejecta ($\rho_{SN} \propto r^{-n}$); for the CSM density distribution created by steady-state mass loss ($s = 2$), the predicted expansion rate is $m = 0.875$ (for an ejecta slope $n = 10$) or 0.8 (for $n = 7$) (Chevalier 1982). Then, in adopting $p = 3$, we expect that the temporal slope in the synchrotron emission is described by $\beta = -1.375$ (for $n = 10$) or -1.6 (for $n = 7$) in the adiabatic regime (e.g., Maeda 2013a).

---

[27] They are also marginally consistent with SNe IIn. However, the distribution of SNe IIn extending down to ~ 200 days is driven by rare outliers (see Figure 5 of Bietenholz et al. 2021).

Table 2
Characteristics of the Synchrotron Emission

Indices	Params.	Synchrotron	Adiabatic
α	...	$-\dfrac{p}{2}$	$\dfrac{1-p}{2}$
β	...	$\dfrac{((2p+16)-(p+2)s)m-2p-8}{4}$	$\dfrac{((2p+22)-(p+5)s)m-2p-10}{4}$
α	$p=3$	$-\dfrac{3}{2}$	-1
β	$p=3$	$\dfrac{(22-5s)m-14}{4}$	$(7-2s)m-4$
α	$p=3$, $s=2$	$-\dfrac{3}{2}$	-1
β	$p=3$, $s=2$	$(3m-3)-\dfrac{1}{2}$	$(3m-3)-1$

Note. The spectral index and temporal slope parameters α and β ($L_\nu \propto \nu^\alpha t^\beta$) are given as a function of the electron distribution power-law index p, the evolution of the forward shock (FS) m ($R \propto t^m$), and the power-law index of the CSM density distribution s ($\rho_{CSM} \propto r^{-s}$).

This is consistent with the late-time ($\gtrsim 17$ days) decay slope at 100 GHz. The decay at 250 GHz is slightly flatter, indicating that it is in the cooling regime at least on day 17; if the electrons are in the synchrotron cooling regime, the decay slope is flatter (by 0.5 for $s=2$) in the corresponding frequency (Björnsson & Fransson 2004; Maeda 2013a). Therefore, if the accelerated electrons are initially in the cooling regime, and then later enter into the adiabatic regime, a decay slope slightly flatter than the adiabatic expectation is recovered. Indeed, Figure 3 suggests that the emission is initially in the cooling regime (i.e., on day 17) even at 100 GHz, and thus the flattening by the cooling effect must be at work even at 100 GHz; therefore the CSM distribution responsible for the late-time emission is likely steeper than $s=2$.

The flat evolution in the earlier phase at 250 GHz ($\lesssim 17$ days) cannot be explained by assuming the same CSM slope as in the later phase ($\gtrsim 17$ days). From the light-curve modeling of the ALMA data (Section 4), we find that the synchrotron cooling dominates over the inverse Compton (IC) cooling for SN 2018ivc. In this case, the maximally allowed change in the decay slope is 0.5 for $s=2$ under the extreme assumption that the earlier and later phases are fully in the cooling and adiabatic regimes, respectively. The observed change in the slope is larger, and thus cannot be attributed solely to the cooling effect.[28]

The above analyses motivate us to revisit the theoretically expected decay slope. Table 2 shows the expected characteristics of the synchrotron emission from the SN–CSM interaction in the optically thin regime, which is an extension of Maeda (2013a) but with s taken as a free parameter. Figure 6 shows the expected temporal slope (β) as a function of the CSM density distribution (s), where the shock wave expansion rate (m) is taken either from the self-similar solution (with $n=7$ and 10; Chevalier 1982) or as a free expansion. The observed slopes for SN 2018ivc in the early and late phases are shown for comparison.

It is clear that the change in decay rate seen in SN 2018ivc is not reproduced merely by the transition from the cooling regime to the adiabatic regime. For example, if we adopt $n=10$, $s \sim 2$ is required if the late-phase slope is to be
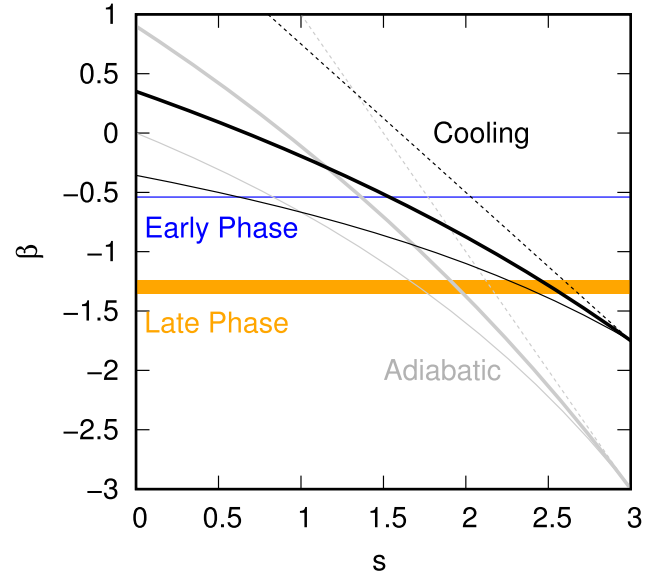
Figure 6. The expected temporal slope (β) in the optically thin synchrotron emission powered by the SN–CSM interaction, as a function of the CSM density slope (s). Two cases are shown, one for the adiabatic regime (gray) and one for the synchrotron cooling regime (black). For each case, three curves are shown in which either a free expansion solution (dashed) or a self-similar expansion solution for an ejecta slope of $n=7$ (thin solid) or $n=10$ (thick solid) is adopted. The observed temporal slopes (β) are shown for the early ($\lesssim 17$ days) and late phases ($\gtrsim 17$ days).

explained by the adiabatic solution, whereas $s \sim 1.5$ is necessary if the early-phase slope is to be explained by the cooling solution. Indeed, if the effect of the cooling is substantial even in the late phase, then $s \sim 2.5$ is required in the late phase. The analysis here clarifies that the CSM density distribution must deviate from a single power law in order to explain the entire light-curve evolution, such that the inner CSM is flat ($s \lesssim 2$) and the outer CSM is steep ($s \gtrsim 2$).

4. Radio Emission Models

To further constrain and quantify the properties of the SN ejecta and the CSM, we compute the synchrotron emission originating in the SN–CSM interaction. We adopt the same formalism used by Maeda et al. (2021). The model assumes that the synchrotron emission can be fully attributed to relativistic primary electrons accelerated at the FS; for the situation under consideration, the contribution from secondary electrons is negligible (see Appendix).

Given the similarity to SN IIb 1993J in radio peak properties, we have adopted a typical ejecta structure for an SN IIb: $M_{ej}=3M_\odot$, $E_K=1.2\times10^{51}$ erg, and an outer density structure with $n=10$ with constant inner density. The ejecta mass adopted here is similar to that adopted in models for SN 1993J including ~ 0.5–$1M_\odot$ of the H-rich envelope (Nomoto et al. 1993; Shigeyama et al. 1994; Woosley et al. 1994). The CSM structure is described as $\rho_{CSM}=Dr^{-s}=10^{-14}D'(r/5\times10^{14}\,\mathrm{cm})^{-s}$ g cm^{-3}, where the density scale (D or D') and the slope (s) are the input parameters we want to constrain by comparing the model light curves with the observed ones. The corresponding mass-loss rate at 5×10^{14} cm is given by $\dot{M}\sim 10^{-3}D'(v_w/20\,\mathrm{km\,s^{-1}})M_\odot$ yr^{-1}.

With regard to the microphysical parameters, the power-law index of the energy distribution of the accelerated electrons (p) can be constrained robustly from the SED evolution, and is

---

[28] Adopting IC cooling would not remedy the situation as the optical luminosity is nearly constant in the early phase, and the predicted change in slope is even smaller than that in the synchrotron cooling regime (Maeda 2013a).

Table 3
Radio Synchrotron Model Parameters and Characteristics[a]

Model	s_{in}	D'_{in}	s_{out}	D'_{out}	ϵ_e	ϵ_B	Radio?[b]	Optical & X-Ray?[c]	Note
A	1.6	0.24	2.5	0.68	0.004	0.012	Yes	Yes	Final model
A′	…	…	2.0	0.2	0.004	0.012	No	No	Steady-state mass loss
B	1.6	0.02	2.4	0.06	0.04	0.02	Yes	No	Radio-only model

Notes.
[a] s_{in} and D'_{in} are the CSM properties at $\lesssim 2 \times 10^{15}$ cm (the early phase), while s_{out} and D'_{out} are those at $\gtrsim 2 \times 10^{15}$ cm (the late phase).
[b] Does the model provide a reasonable fit to the ALMA data?
[c] Does the model provide a reasonable fit to the optical–NIR bolometric light curve and the X-ray flux?

fixed as $p = 3$ (Section 3.3). For the absorption processes, both the synchrotron self-absorption within the shocked region and the free–free absorption in the unshocked CSM are included. The effect of the free–free absorption is however uncertain; we simply assume a constant electron temperature in the unshocked CSM, and treat this as an additional input parameter.

We further assume that the fractions of energy dissipated at the FS going into the accelerated electrons (ϵ_e) and into the amplified magnetic field (ϵ_B) are constant in time. We note that there is a degeneracy between these parameters and the CSM density such that they give rise to similar (or identical) radio light curves, and it is not always possible to derive a unique set for these parameters separately based on analysis of the radio emission alone. We thus vary these parameters along with the CSM density/structure in investigating the properties of SN 2018ivc. In what follows, we present two choices for the combination of ϵ_e and ϵ_B: in Model A, we adopt $\epsilon_e = 0.004$ and $\epsilon_B = 0.012$, while in Model B we adopt $\epsilon_e = 0.04$ and $\epsilon_B = 0.02$. The choice in Model B is straightforward; here, we fix these parameters to the same values adopted in the model for SN Ic 2020oi (Maeda et al. 2021),[29] noting however that it is unclear whether these microphysical parameters are universal or not for different SNe with different CSM densities and shock velocities. The reason for the choice in Model A will become evident later in Section 5, where we investigate the possibility that the same SN–CSM interaction model (with the same SN ejecta and CSM properties) can also explain the optical and X-ray light curves; this is motivated by the close similarity between the evolution of the radio light curves and that of the optical (bolometric) light curve (Figure 4).

Given the issues identified with a single CSM structure in Section 3.3, we model the early- and late-phase light curves separately, allowing for different CSM distributions but fixing the other parameters (ejecta properties and microphysical parameters) to the same value between the two phases. The validity of the separate modeling between different temporal windows has been justified by Maeda et al. (2021) for SN Ic 2020oi, in which qualitatively similar CSM structures, i.e., an inner flat region plus an outer steep region, were considered. For a given set of ϵ_e and ϵ_B, we thus derive the CSM parameters (s and D') that produce synthetic radio light curves consistent with the ALMA data. In addition, we simulate a single and smooth CSM structure corresponding to steady-state mass loss over the entire scale (i.e., by adopting the same CSM structure for the early and late phases), and denote this as Model A′.

Figure 7. The light curves for Models A (red and blue solid lines), A′ (dashed lines), and B (gray solid lines), as compared to the ALMA light curves of SN 2018ivc at 100 GHz (red open squares) and 250 GHz (blue filled squares). Note that the curves for Model B largely overlap with those for Model A.

The models presented in this paper are summarized in Table 3, while Figure 7 shows the model radio light curves. Models A and B adopt separate modeling between the early and late phases, and thus the model curves are only loosely connected at ∼17 days, corresponding to ∼2×10^{15} cm. The CSM density scale (D') in Model A′ is set so that the overall radio flux scale in the ALMA data is reproduced. Model A′ however predicts essentially a single-power-law light-curve behavior in the optically thin phase and never explains the characteristic temporal evolution found for SN 2018ivc. The model thus confirms the need for different properties of the CSM in the inner and outer regions, as previously argued in Section 3.3.

Models A and B provide synthetic radio light curves that are nearly identical, as the derived slopes in the CSM distribution (s in the inner and outer components) for the different sets of ϵ_e and ϵ_B are so similar, and it is mainly the absolute flux scale that is affected by changes in the microphysical parameters. On the other hand, the derived CSM density scale (D') is smaller by a factor of ∼10 in Model B compared with Model A. In the rest of this section, we will first investigate the need for a nonsmooth CSM distribution, and then discuss the cause of the degeneracy and a possible way to overcome it.

Figure 8 shows the radio light curves of Model A shown separately in the early and late phases. We adopt an electron temperature of 4×10^6 K, higher than the value frequently

---

[29] In Maeda et al. (2021), these efficiencies were normalized by the "shocked" CSM density. However, it is more appropriate to normalize them by the pre-shock density. The values mentioned here take into account this correction.
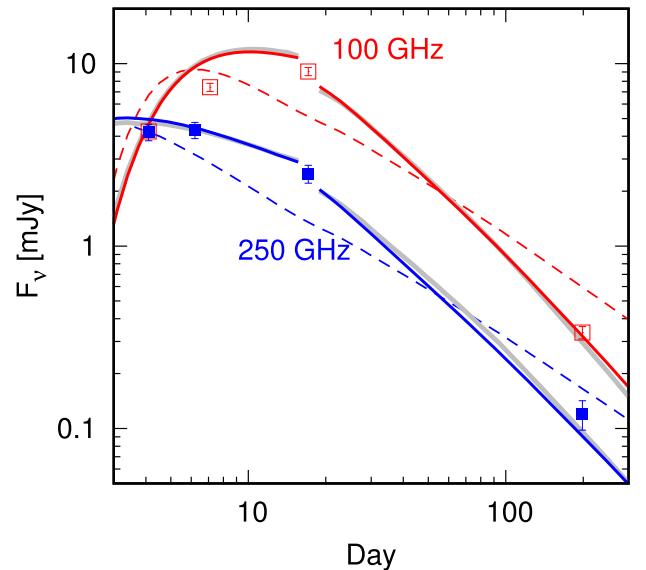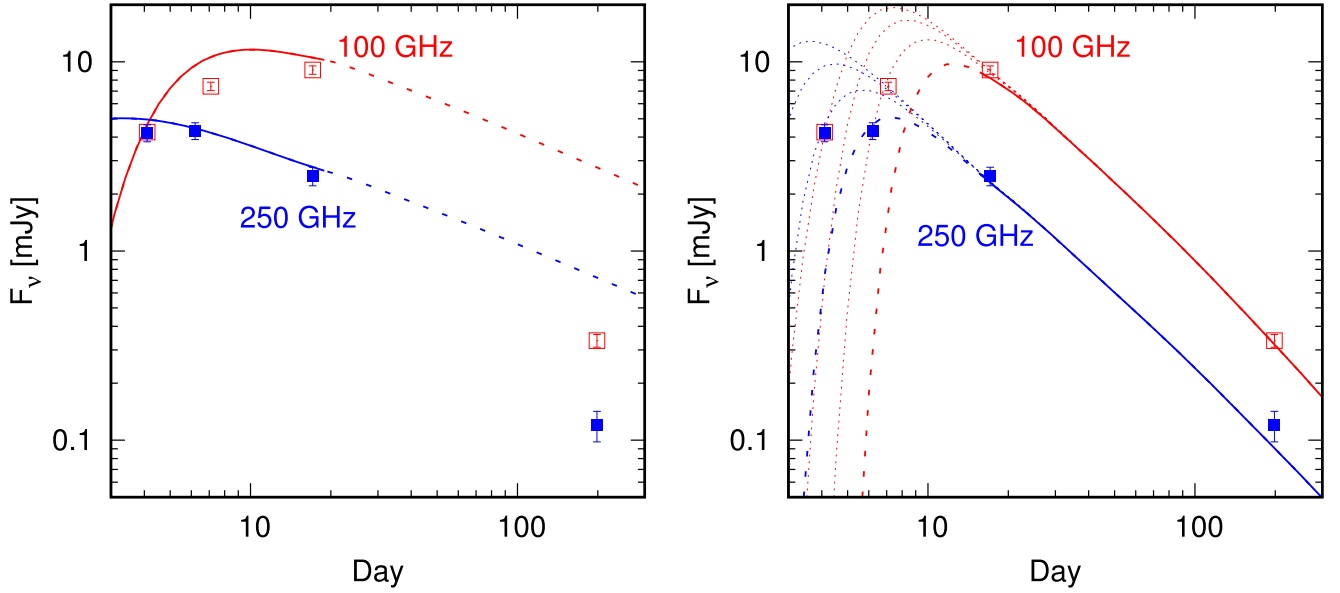
Figure 8. Model A, as compared to the ALMA light curves of SN 2018ivc. The left panel is for the early phase before the optical break ($\lesssim 20$ days), and the right panel is for the late phase after the break. A (relatively) flat CSM density distribution ($\rho_{\rm csm} \propto r^{-1.6}$) below the transition radius ($\sim 2 \times 10^{15}$ cm) is adopted for the early-phase model, while a steep CSM ($\propto r^{-2.5}$) above the transition radius is adopted for the late phase. For the late phase, four models with different pre-shock electron temperatures are shown (4×10^6 K in the thick lines; 0.8, 1.6, 3.2 $\times 10^7$ K in the thin lines). Each model applies only to the period shown by the solid lines; the dashed lines show the prediction for the case where the same CSM distribution would extend above/below the transition radius.

adopted ($\sim 10^5$ to a few 10^6 K; e.g., Fransson & Björnsson 1998). We note however that the investigation of ionization/thermal structures has been limited to a few specific SNe. We postpone further investigation of the effect of free–free absorption to the future. It is seen in Figure 8 that the extrapolation of the late-time model to the earlier phase never reproduces the observed fluxes or SED evolution, irrespective of the assumptions made for free–free absorption. We thus conclude that a different CSM structure, in particular a different density slope, is required for the inner CSM component, reinforcing the arguments in Section 3. Figures 8 and 9 show that the flatter CSM distribution we adopt ($s = 1.6$) can simultaneously explain both the early-phase light curves at 100 and 250 GHz and the SED evolution reasonably well.

The degeneracy between the microphysical parameters and the CSM density scale (i.e., Model A versus Model B) is partly attributed to the main cooling process under the present situation. From the radio modeling of SN 2018ivc we find that the synchrotron cooling dominates over the IC cooling in both Models A and B, due to the high CSM density and relatively low optical luminosity, i.e., a higher ratio of the magnetic field energy density to the seed photon energy density. A comparison with the case of SN Ic 2020oi is instructive, for which IC cooling is found to be the dominant cooling process (Horesh et al. 2020; Maeda et al. 2021). The optical peak luminosity of SN 2018ivc is lower than that of SN 2020oi by a factor of a few for our fiducial value of the extinction (Section 5). On the other hand, the CSM density found for SN 2018ivc is higher than that for SN 2020oi by a factor of at least a few (Model B) or even of ~ 30 (Model A). The ratio of the synchrotron cooling timescale to the IC cooling timescale is $\propto (L_{\rm opt}/R^2)/B^2$, where $L_{\rm opt}$ is the optical luminosity, R is the shock radius, and B is the magnetic field strength. Given that $B^2 \propto \rho_{\rm CSM}$, we estimate that the ratio is lower by a factor of at least ~ 10 for SN 2018ivc, pointing to the importance of the synchrotron cooling.

For SN 2020oi, the dominance of the IC cooling helps in constraining the microphysical parameters, as it introduces an additional dimensional scale to the problem to be solved based on the observational data (i.e., the number of photons; Maeda 2012; Maeda et al. 2021). This is not the case for SN 2018ivc. However, there is an interesting possibility for SN 2018ivc to place an additional constraint if the optical light curve is also powered by the SN–CSM interaction. Model A, our final model, is constructed in this way and this issue is further investigated in the next section.

5. SN–CSM Interaction Model for the Optical and X-Ray Emission

As shown in the previous sections, analysis of the ALMA data suggests that there is a change in the properties of the CSM at ~ 20 days after the explosion, corresponding to $\sim 2 \times 10^{15}$ cm. It is striking that the optical light curve changes its decay rate around the same epoch in a similar manner (Figure 4; see also Bostroem et al. 2020): a relatively flat evolution before ~ 20 days, and steeper decay thereafter. A strong X-ray signal has also been detected on 2018 December 5.7 UT, which is ~ 13 days from the putative explosion date adopted in the present work. Bostroem et al. (2020) suggested that the SN–CSM interaction plays at least a partial role in shaping the optical appearance of SN 2018ivc. Indeed, SN 2018ivc is strikingly similar to the peculiar SN 1996al including the optical light-curve characteristics (Figure 1), for which the SN–CSM interaction model was constructed (Benetti et al. 2016). The spectral properties of SN 2018ivc also support the importance of the SN–CSM interaction (Dessart & Hillier 2022).

We have conducted optical light-curve modeling for SN 2018ivc under the SN–CSM interaction scenario. We are particularly interested in the possibility that the multiwavelength emission might be explained mainly by the SN–CSM interaction; the modeling approach here is thus based on this
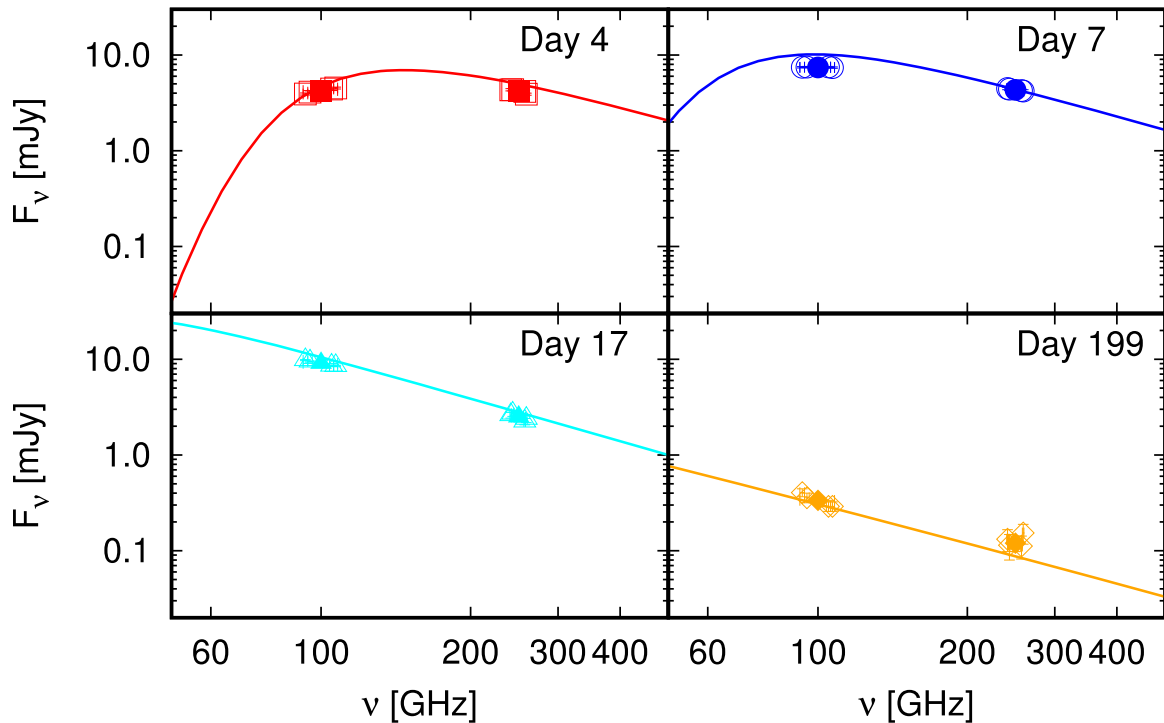
Figure 9. The SED evolution in Model A as compared to the ALMA data.

hypothesis, and especially on the assumption that the contribution by ^{56}Ni/Co heating is negligible. If such a solution exists we will regard it as strong support for the dominance of the SN–CSM interaction as the power source. However we note that this does not immediately exclude some contribution from ^{56}Ni/Co heating (Section 6.1); adding this contribution can change the derived properties of the CSM to some extent, and this caveat must be borne in mind.

Below we provide a brief summary of the model framework and underlying assumptions; see Maeda & Moriya (2022) for a full description of the model (see also Chugai 2001, 2009). We have adopted the same ejecta and CSM structures used in the radio modeling (Models A, A′, and B). The treatment of the shock wave dynamics is basically identical with the radio modeling; we include not only the FS but also the reverse shock (RS) in the optical light-curve model. Several timescales and optical depths are computed for the FS, RS, unshocked ejecta, and unshocked CSM (Figure 10). These are used to characterize the properties of the resulting optical emission. As in the radio modeling, the early and late phases are computed separately for Models A and B. Therefore, these models are not reliable in the transition phase (i.e., ~20–30 days); this is the reason why the model quantities are not plotted in the transition phases in Figures 10–13.

Figure 10 clarifies the main physical processes involved in shaping the optical light curve of SN 2018ivc in our SN–CSM interaction model. To start with, we note that the power input by the FS dominates over that by the RS (Maeda & Moriya 2022). The FS does not reach the cooling regime ($t_c(FS) > t_{dyn}$) from the beginning, and it originally emits hard X-ray photons of ~100 keV. The FS is optically thin to these high-energy photons ($\tau_{100}(FS) < 1$); therefore we assume that half of the power generated at the FS escapes as hard X-ray emission outward, while the other half penetrates inward. Most of the inward-directed hard X-ray photons are absorbed within

the outermost ejecta ($\tau_{100}(RS) \lesssim 1$ and $\tau_{100}(ejecta) \gg 1$). The power input from the RS behaves differently; the RS is quickly cooled down and emits optical photons ($t_c(RS) < t_{dyn}$ and $\tau_1(RS) \gg 1$). The ion–electron equipartition is justified during most of the period modeled in the present work, except for the latest phase ($\gtrsim 100$ days).

The model optical (bolometric) light curve thus computed is shown in Figure 11, as compared to the bolometric light curve constructed by A. Reguitti et al. (2022, in preparation) with data collected from various telescopes including the Subaru Telescope equipped with the Faint Object Camera and Spectrograph (FOCAS) under the proposal S19B-055; details will be presented by A. Reguitti et al. (2022, in preparation). The composition of the light curves for Model A (i.e., our final model) is described in Figure 12. We note that the extinction within the host galaxy is substantial, with a large uncertainty. In the present work we adopt the "low-extinction" case in A. Reguitti et al. (2022, in preparation) with $E(B-V) \sim 0.5$ mag and $R_V \sim 3$ (Cardelli et al. 1989); this case is similar to the one adopted by Bostroem et al. (2020).[30]

In adopting a single-power-law CSM distribution with $s = 2$ (i.e., steady-state mass loss), Model A′ does not reproduce the optical–NIR bolometric light curve of SN 2018ivc (Figure 11). Models A and B, which result in nearly identical radio light curves (Section 4), predict very different behaviors in the optical–NIR bolometric light curves. Thus, if we assume that both the radio and optical light curves should be explained by the same SN–CSM interaction model, we can solve the degeneracy between the microphysical parameters and the CSM scale encountered in the radio modeling alone. In particular our Model A can produce a reasonable match to both the radio and optical light curves simultaneously. While it is

---

[30] We have also applied the radio–optical combined model (similar to Model A) for the case with high extinction ($E(B-V) \sim 1$ mag); the effect will be shown in Section 6.2 for the derived CSM density.
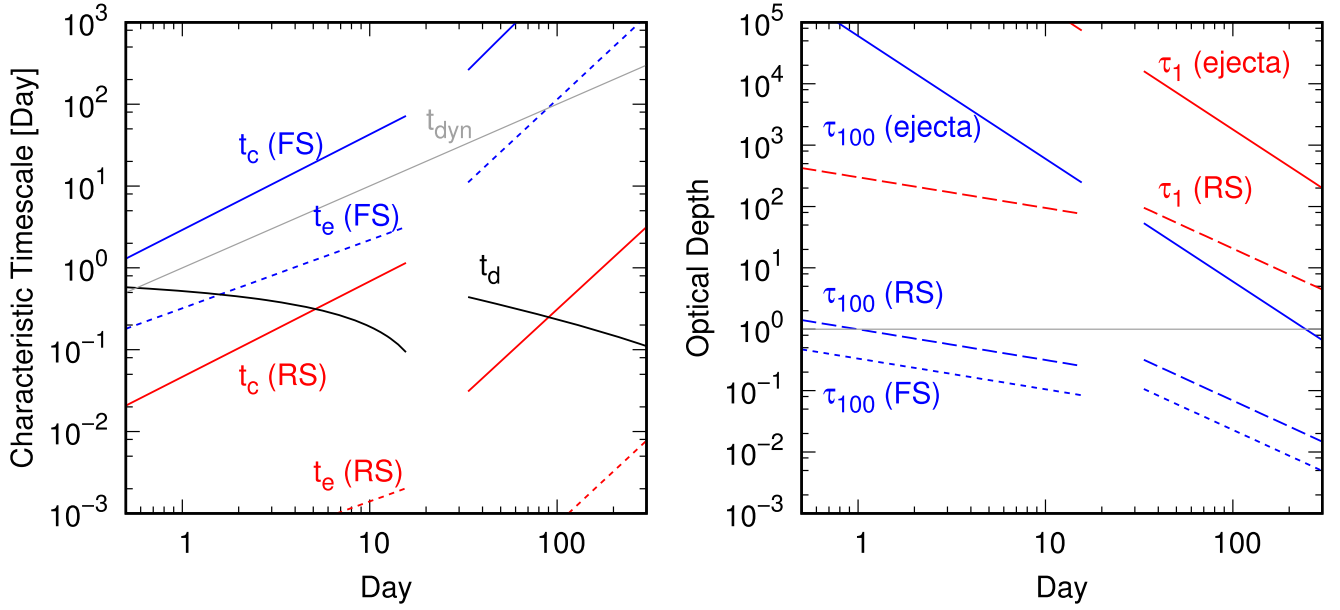
Figure 10. The characteristic timescales (left) and optical depths (right) found in Model A. Shown in the left panel are the dynamical timescale ($t_{\rm dyn}$; gray), the diffusion timescale of the optical photons ($t_{\rm d}$; black), the cooling timescale ($t_{\rm c}$; solid lines), and the electron–ion equipartition timescale ($t_{\rm e}$; short-dashed lines) in the FS (blue) and RS (red) regions. The optical depths shown in the right panel are as follows: the photons at ∼100 keV originally emitted at the FS (τ_{100}) traveling in the FS (blue short-dashed lines), the RS (blue long-dashed lines), or the ejecta (blue solid lines). The same is shown for the photons at ∼1 keV originally emitted at the RS (τ_1, shown by red lines).
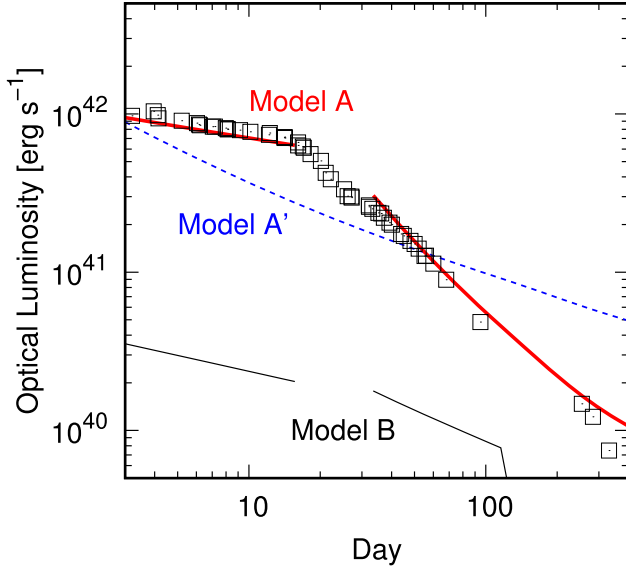
Figure 11. The bolometric light curve of SN 2018ivc (black open squares), as compared to the synthetic light curves computed for Models A (red thick line), A′ (blue dashed line), and B (black thin line).

Figure 12. The light curves computed for Model A. The individual contributions by the FS and RS are shown by the blue and red lines, respectively. The dissipation rate of the kinetic energy is shown by the magenta dashed line. The maximum contribution by the ^{56}Ni/Co decay is shown by the gray line (for which the phase before the peak is shown by the dashed line; the simple optical light-curve model here does not apply in the premaximum phase: Maeda & Moriya 2022), including the effect of the decreasing optical depth on the decay γ-rays (Maeda et al. 2003).

still possible that the optical emission could in fact be powered by a different mechanism, e.g., the ^{56}Ni/Co heating, given the very different emission processes in the optical and radio even if we consider only the SN–CSM interaction, we regard the success of Model A as significant.

It is worth noting that there is no free/tunable parameter within the SN–CSM interaction model framework that guarantees that the radio and optical light curves can be fit simultaneously; this strongly indicates that the model captures the basic physical scenario realized in SN 2018ivc. For example, Figure 11 highlights that Model B differs from the optical light curve not only in the flux level, but also in the (flatter) evolution in the late phase; this is due to the low CSM density leading to a
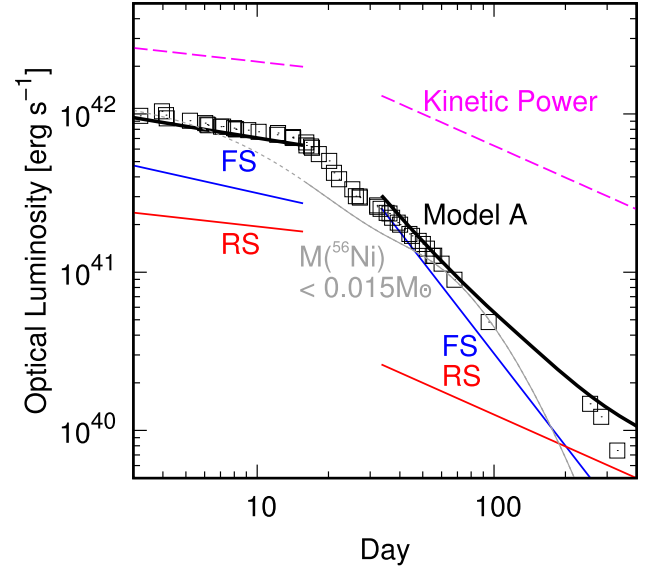
transition of the main power source from the FS to the RS (Maeda & Moriya 2022). When the higher CSM density of Model A is adopted, both the predicted flux and its evolution become much more consistent with the observed light curve.

Further diagnostics can be obtained through the X-ray emission. SN 2018ivc was detected by the Chandra X-Ray Observatory equipped with the Advanced CCS Imaging Spectrometer (ACIS) (Bostroem et al. 2020). Its flux corresponds to ∼10^{40} erg s^{-1} in the 0.5–8 keV energy band at a distance of
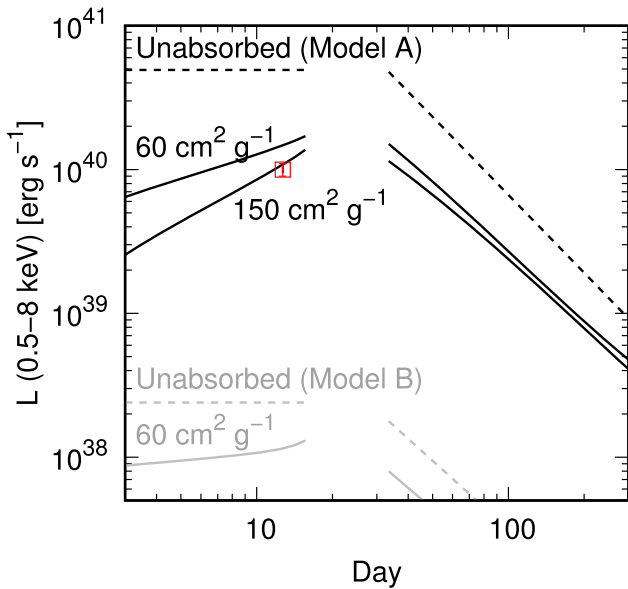
Figure 13. The X-ray (0.5–8 keV) light curves of SN 2018ivc predicted from Model A (black) and Model B (gray). The Chandra observation is shown by the red open square (Bostroem et al. 2020). For each model, the intrinsic 0.5–8 keV luminosity without any absorption within the CSM is shown by the dashed lines. The predicted light curves are shown by the solid lines, assuming a photoelectric absorption opacity of 60 or 150 cm^2 g^{-1} at 1 keV.

10.1 Mpc. The same SN–CSM interaction model applied to the optical light curve also predicts the X-ray flux as an output (Maeda & Moriya 2022), which is compared to the observed flux in Figure 13.

Since the RS is in the cooling regime, the X-ray emission is entirely attributed to the FS in this model. This is dominated by the free–free emission, and thus (unabsorbed) f_ν is constant up to ~100 keV. This suffers from extinction within the unshocked CSM in the 0.5–8 keV band through photoelectric absorption, the opacity of which is assumed to be $\kappa_E = \kappa(1\ \mathrm{keV})(E/1\ \mathrm{keV})^{-8/3}$. Adopting $\kappa(1\ \mathrm{keV}) = 60\ \mathrm{cm}^2\ \mathrm{g}^{-1}$ as roughly describing the solar metal composition, we see a reasonable match between the predicted flux of Model A and the observed one. The agreement is even better if we adopt $\kappa(1\ \mathrm{keV}) = 150\ \mathrm{cm}^2\ \mathrm{g}^{-1}$, which corresponds to the slightly C-rich composition ($X(\mathrm{C}) \sim 0.1$) expected for the He-enriched CSM in case the mass loss has penetrated down near to the bottom of the H-rich envelope (i.e., the case for SNe IIb). On the other hand, Model B cannot provide a sufficiently strong X-ray signal, irrespective of the treatment of absorption; even the unabsorbed flux is already below the observed flux, indicating that the CSM density is too low for this model to explain the detected X-ray flux.

Furthermore, the CSM density cannot differ much even if we were to consider an ^{56}Ni/Co contribution to the optical emission. There is little doubt that the X-ray emission originates in the SN–CSM interaction. The shock is in the adiabatic regime, and thus the X-ray luminosity scales as ρ_{CSM}^2. Even considering the extreme case of no attenuation of the X-ray emission within the CSM, the CSM density cannot be lower than that in Model A by more than a factor of 2 in order to account for the observed X-ray emission.

In summary, it is possible to explain all of the multiband radio light curves, the optical bolometric light curve, and the X-ray detection/flux using the same SN–CSM interaction scenario of our Model A. It would be too much of a

coincidence if there were no connection in the underlying processes. We thus suggest that the optical emission from SN 2018ivc, as well as the radio and X-ray emission, is primarily powered by the SN–CSM interaction. In this interpretation, this is a rare example in which the multiwavelength emission from an SN is powered mainly by the SN–CSM interaction; it is believed to be so for SNe IIn, but a combined analysis like this across all these wavelengths for other subtypes has been quite rare (e.g., Margutti et al. 2014, 2017).

From the radio peak properties (Section 3.1) we adopt the ejecta properties (the ejecta mass and the kinetic energy) typical of SNe IIb, choosing the combination widely accepted for SN 1993J. In this section we have shown that the multiwavelength properties are indeed recovered by such a model. In the proposed interpretation, this is potentially the first example where the multiwavelength emission from an SN whose ejecta are indeed similar (or identical) to those of "canonical" SNe IIb (or SESNe in general) is powered entirely by the SN–CSM interaction.[31] We cannot rule out the possibility that the optical emission is substantially contributed by ^{56}Ni/Co decay, while the radio and X-ray emissions are powered by the SN–CSM interaction. The usual situation in canonical SESNe is that a multiwavelength fit is generally not possible with the SN–CSM interaction alone (Fransson & Björnsson 1998). Nevertheless, even in such a situation the subsequent discussion (Section 6) based on the derived CSM properties of SN 2018ivc would not be affected, since the X-ray analysis alone can place a strong lower limit on the CSM density.

6. Implications for the Origin of SN 2018ivc

6.1. The SN Properties: SN IIb with an Extended H-rich Envelope?

Our analyses presented in Sections 3–5 demonstrate that SN 2018ivc most closely resembles an SN IIb in terms of a progenitor and its explosion. However its peculiarities, especially in the optical light curve, are best explained by a difference in the CSM density scale, where the high CSM density for SN 2018ivc leads to the optical emission (plus radio and X-rays) being mainly powered by the SN–CSM interaction.

SN 2018ivc nevertheless showed strong (emission-dominated) hydrogen lines throughout its evolution, which is different from the spectral evolution of SNe IIb. While modeling of the optical spectra is beyond the scope of the present paper, we note that this apparent contradiction can be reconciled by one or more of the following: (1) broad (and boxy) H and He emission lines were seen to emerge for SNe IIb 1993J (Matheson et al. 2000a, 2000b), 2013df (Maeda et al. 2015), and ZTF 18aalrxas (Fremling et al. 2019) ~200–300 days after the explosion when the SN–CSM interaction started dominating the optical output; (2) SN 2018ivc is likely a transitional object between IIb and IIL, such that SN 2018ivc probably has a more massive H-rich envelope than SN 1993J; and (3) Dessart & Hillier (2022) have recently shown that SN ejecta interacting with moderately dense H-rich CSM can create broad emission lines as seen in SN 2018ivc.

---

[31] SNe Ibn are also an example for which the progenitor is probably an He star powered by the SN–CSM interaction (Pastorello et al. 2007); however, SNe Ibn are unlikely to share the progenitor properties of the usual SNe IIb and SESNe (Maeda & Moriya 2022).

We can place a rough upper limit on the mass of the H-rich envelope on the basis of the optical light curve. Under standard stellar evolution including both single and binary models, an SN progenitor undergoes an extended giant phase with an H-rich envelope mass of $\gtrsim 0.15 M_\odot$, as set by the hydrostatic condition (Ouchi & Maeda 2017). A consequence of this is that the light-curve plateau that characterizes SNe IIP lasts longer for a more massive H-rich envelope (e.g., Popov 1993; Kasen & Woosley 2009; Martinez et al. 2022). For an H-rich envelope mass exceeding $\sim 1.5 M_\odot$, the plateau length becomes $\gtrsim 20$ days (Hiramatsu et al. 2021), which is the stage when the optical light curve of SN 2018ivc began a rapid decay.

The proposed SN IIb interpretation also requires that the ^{56}Ni heating not be a significant power source for the optical luminosity. This constrains the ^{56}Ni mass ejected by SN 2018ivc to $\lesssim 0.015 M_\odot$ (Figure 12). The ^{56}Ni mass estimated for SN 1993J is $\sim 0.07 M_\odot$ (Nomoto et al. 1993; Woosley et al. 1994), which is larger than the upper limit for SN 2018ivc by a factor of ~ 4–5.[32]

This poses the question as to whether such a small mass of ^{56}Ni is consistent with the SN IIb interpretation. Our upper limit is substantially smaller than the typical values found for a sample of SNe IIb observed to date (Anderson 2019; Meza & Anderson 2020; Afsariardchi et al. 2021). However, for SESNe including SNe IIb, there is a potential selection bias in which SNe with a large amount of ^{56}Ni are preferentially discovered; the intrinsic distribution of $M(^{56}$Ni$)$ for a sample of SESNe, including SNe IIb, may then be more similar to that of SNe IIP (Ouchi et al. 2021), in which $0.015 M_\odot$ of $M(^{56}$Ni$)$ is not really an outlier (Rodríguez et al. 2021). Indeed, there are increasing indications that SNe IIb with a relatively small amount of ^{56}Ni exist as a population of rapidly evolving transients (Ho et al. 2021) and/or as underluminous SNe IIb (e.g., SN 2017czd with $M(^{56}$Ni$) \lesssim 0.003 M_\odot$ (Figure 1; Nakaoka et al. 2019). We conclude that the scenario of SN 2018ivc as an SN IIb cannot be rejected on the basis of the $M(^{56}$Ni$)$, and indeed if SN 2018ivc did not have such a dense CSM it might simply have been classified as a faint and rapidly evolving SN IIb.

Based on the nondetection of a progenitor to SN 2018ivc in pre-SN Hubble Space Telescope images, Bostroem et al. (2020) concluded that the ZAMS mass must have been either $\lesssim 12 M_\odot$ or $\sim 50 M_\odot$, suggesting the low-mass interpretation is more likely. This is also consistent with the SN IIb scenario for SN 2018ivc. The upper limit, $M_{\rm ZAMS} \lesssim 12 M_\odot$, is within the range expected for SNe IIb in the binary evolution scenario, and a progenitor in this mass range has been found for SN IIb 2016gkg (Tartaglia et al. 2017; Kilpatrick et al. 2022).

SNe IIb appear to form a diverse population in terms of the properties of the H-rich envelope (radius and mass) still intact at the time of the explosion, covering the range from blue supergiant (with a radius of $\lesssim 50 R_\odot$ for SN 2008ax; Folatelli et al. 2015) through yellow supergiant (YSG; $\sim 200 R_\odot$ for SNe 2011dh and 2016gkg; Maund et al. 2011; Tartaglia et al. 2017; Bersten et al. 2018) to RSG ($\sim 600 R_\odot$ for SNe 1993J, 2013df, and ZTF 18aalrxas; Maund et al. 2004; Van Dyk et al. 2014; Fremling et al. 2019). In the absence of a direct progenitor detection, the progenitor radius of SN 2018ivc is not known. However, there are a few indications that favor an extended RSG progenitor for SN 2018ivc: (1) the peak radio properties,
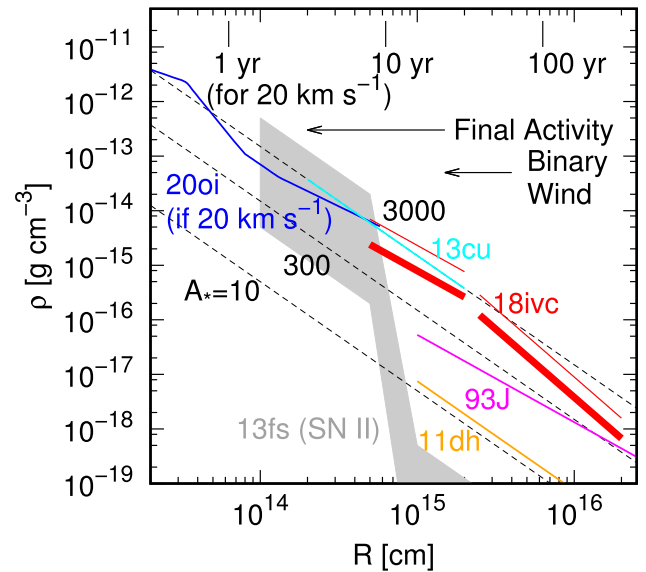

Figure 14. The CSM structure estimated for SN 2018ivc by combined analysis of the radio, optical, and X-ray light curves (Model A; red thick line). Also shown is a similar model, but for the high-extinction case (red thin line). For comparison, the CSM distributions for SNe IIb 1993J (magenta), 2011dh (orange), and 2013cu (cyan), as well as those for SN IIP 2013fs (gray band) and the scaled SN Ic 2020oi (blue), are shown. The CSM corresponding to steady-state mass loss is shown for three choices of the CSM density scale (A_* as defined by $\rho_{\rm CSM} = 5 \times 10^{11} A_* r^{-2}$ g cm^{-3}; $A_* \sim 1$ for $\dot{M} = 10^{-5} M_\odot$ yr^{-1} and $v_{\rm w} = 1000$ km s^{-1}). Shown at the top is the pre-SN lookback time for $v_{\rm w} = 20$ km s^{-1}.

suggested to be correlated with the progenitor radius (Chevalier & Soderberg 2010), are more similar to those of SN 1993J than to those of other SNe IIb with a less extended progenitor envelope (Section 6.3), and (2) the early optical/UV emission within the first few days, which can provide an indication of the progenitor radius, also resembles that of SN 1993J (Figure 1; Section 6.4).

SNe II and SNe IIb form distinct classes in terms of their observational properties, and events that bridge the observed properties of SNe II and IIb are few in number (Pessi et al. 2019). The rarity of such events, including SN 2018ivc as suggested here, may well be understood in terms of the binary interaction scenario toward SNe IIb (Section 6.3). We note that the peculiar SN II 2013ai has recently been suggested to have ejecta properties similar to those of SN 1993J and to be a link between SNe II and SNe IIb (Davis et al. 2021). However, SN 2013ai shows observational properties different from those of SN 2018ivc (and its cousin SN 1996al); in particular, the light-curve model suggests a large amount of ^{56}Ni (0.3–$0.4 M_\odot$) for SN 2013ai. We also note that the environment of SN 2013ai suggests a much more massive progenitor with $M_{\rm ZAMS} \sim 17 M_\odot$ (Davis et al. 2021) compared to that of SN 2018ivc.

6.2. The Inner CSM Properties: Pre-SN Dynamical Activity?

Figure 14 shows the CSM density structure around SN 2018ivc, derived from Model A. To evaluate the uncertainty associated with the extinction within the host galaxy, we have performed the same exercise but adopting the high-extinction case with $E(B-V) \sim 1$ mag, confirming that the extinction assumed would not affect the main conclusions.

Assuming a velocity of $v_{\rm w} \sim 20$ km s^{-1} for the material ejected by the pre-SN mass loss, as is typical for SNe IIb with RSG or YSG progenitors (e.g., Groh 2014), the radial scale of

---

[32] In the "high-extinction" case however (A. Reguitti et al. 2022, in preparation), the upper limit will go up to ~ 0.07–$0.08 M_\odot$, and the following discussion does not apply.

the CSM constrained by the present work (between $\sim 5 \times 10^{14}$ cm and 1.5×10^{16} cm) reflects the mass-loss history in the ~ 200 up to 10 yr before the SN explosion. The change in the properties of the CSM structure at $\sim 2 \times 10^{15}$ cm indicates that the mass-loss mechanism might have changed ~ 30 yr before the explosion. The corresponding mass-loss rate is $\sim 1.5 \times 10^{-4} M_{\odot}(v_{\mathrm{w}}/20\,\mathrm{km\,s^{-1}})\,\mathrm{yr^{-1}}$ at $\sim 200-30$ yr before the SN, and $\sim 3 \times 10^{-4} M_{\odot}(v_{\mathrm{w}}/20\,\mathrm{km\,s^{-1}})\,\mathrm{yr^{-1}}$ at $\sim 30-10$ yr.

The inner CSM component may correspond to the "confined" CSM associated with the final activity of a massive star, so far mostly inferred for SNe IIP. For comparison, Figure 14 shows the CSM structure of SN IIP 2013fs (Yaron et al. 2017) (gray-shaded region), which probably has a similar mass-loss wind velocity to those of SNe IIb and SN 2018ivc shown in the same figure. The difference is most striking in the outer region: SN IIP 2013fs has a much lower CSM density at $\gtrsim 10^{15}$ cm, indicating that the mass-loss rate up to ~ 10 yr before its explosion was much lower than those of SNe IIb. SN 2013fs shows a huge jump in CSM density at $\sim 10^{15}$ cm to so-called "confined" CSM, where the CSM density is comparable to that of SN 2018ivc. The CSM structure of SN 2013fs is interpreted as the mass loss being dominated by the usual, steady RSG wind up to ~ 10 yr before the explosion, after which the progenitor experienced additional pre-SN activity in the final ~ 10 yr with a mass-loss rate of $\sim 10^{-5}$ to $10^{-3} M_{\odot}$ $\mathrm{yr^{-1}}$. The cause of this is still under active debate, with a popular suggestion being that it is driven by an accelerated change in the nuclear burning stage in the final phase of the massive star evolution, to which the progenitor envelope reacts within a dynamical timescale (Quataert & Shiode 2012; Fuller 2017; Maeda et al. 2021).

The CSM density scale in the inner CSM component $(\lesssim 2 \times 10^{15}$ cm) of SN 2018ivc is within the range estimated for the confined CSM around SN IIP 2013fs, while the spatial extent is different by a factor of ~ 2. There could be some diversity in the nature of the confined CSM in terms of its mass and radial scale, either in the timing when the final activity sets in or in the energy provided by the core relative to the envelope binding energy (Morozova et al. 2020; Takei et al. 2022). Indeed, the inner CSM component of SN 2018ivc matches well to that derived for SN IIb 2013cu from optical "flash spectroscopy" (Gal-Yam et al. 2014; Groh 2014). We note that these SNe IIP and IIb probably have similar velocities associated with the pre-SN mass loss, allowing a fair and direct comparison of the mass-loss histories of these SNe based on the CSM distribution.

A comparison with the CSM structure around SN Ic 2020oi is also interesting, for which the CSM structure up to $\sim 2 \times 10^{16}$ cm has been derived on the basis of multiband radio data (Maeda et al. 2021). Since it is an SN Ic, we assume $v_{\mathrm{w}} \sim 1000\,\mathrm{km\,s^{-1}}$ for SN 2020oi, and then scale the CSM structure around it as if it would have experienced the same mass-loss history as a function of time, but with $v_{\mathrm{w}} \sim 20$ km $\mathrm{s^{-1}}$. This "scaled" CSM structure for SN 2020oi is shown in Figure 14. The "outer" CSM structure of SN 2020oi shows a good match to the "inner" components of SN IIP 2013fs, SN IIb 2013cu, and SN 2018ivc, strengthening a possible association of the inner CSM component of SN 2018ivc with some "final activity." This suggests a general picture in which the properties of the final pre-SN activity are likely common to SNe IIP and SESNe (including SNe IIb and SN 2018ivc), and

all such activity takes place within the last few decades before the final core collapse.

6.3. The Outer CSM Properties: A Binary Interaction Origin?

We interpret the "outer" CSM component at $\gtrsim 2 \times 10^{15}$ cm as being created by steady evolution characterized by a stellar wind or a binary interaction. Figure 14 shows the CSM structures derived for two representative SNe IIb, SN 1993J from an RSG and SN 2011dh from a YSG. The CSM structures shown here are based on X-ray analysis for SN 1993J (Immler & Wang 2001), and on a combined analysis of the radio and X-rays for SN 2011dh (Maeda 2012; Soderberg et al. 2012; Maeda et al. 2014). Note that for these SNe, a single power law is assumed for the entire CSM radial density distribution, and while the presence of a confined CSM cannot be ruled out, we will focus only on the outer CSM distribution ($\gtrsim 2 \times 10^{15}$ cm) for this comparison.

The difference between SN IIP 2013fs and SNe IIb is clear, with the SNe IIb shown here having a much higher CSM density in the outer region. These SNe IIb are from either a YSG or an RSG progenitor, and thus the velocity of the ejected material is probably similar to that for SN IIP progenitors; thus the difference is most probably in the actual mass-loss rate. This difference can be attributed to the existence of an additional mass-loss process for SNe IIb, namely mass loss originating from a binary interaction (e.g., Ouchi & Maeda 2017; Yoon 2017).

It has been suggested that there is a relationship between the natures of SN IIb progenitors and their CSM, whereby a more extended progenitor tends to be surrounded by a denser CSM (Maeda et al. 2015). This is illustrated by the comparison between SNe 1993J (RSG) and 2011dh (YSG) in Figure 14, and explains the correlation between the progenitor radius and the radio peak properties of SNe IIb (Chevalier & Soderberg 2010). The CSM around the progenitor of SN 2018ivc is even denser than that for SN 1993J, at least by a factor of a few. Under an SN IIb scenario for SN 2018ivc, the progenitor of SN 2018ivc would have been an RSG with an extended and relatively massive H-rich envelope (i.e., $\sim 0.5-1 M_{\odot}$). A binary interaction scenario for SNe IIb naturally explains the diversity in the mass-loss rates as well as the relation between the progenitor radius and the mass-loss rate (Ouchi & Maeda 2017); the initial binary separation is a controlling factor, in such a way that a closer initial orbit results in a less massive and less extended H-rich envelope, as well as in a lower mass-loss rate in the final ~ 1000 yr.

One question is whether the high mass-loss rate for SN 2018ivc is within the range expected in the context of the binary evolution scenario. The estimated mass-loss rate is $\sim 1.5 \times 10^{-4} M_{\odot}(v_{\mathrm{w}}/20\,\mathrm{km\,s^{-1}})\,\mathrm{yr^{-1}}$ in the $\sim 200-30$ yr before the SN. In a particular sequence of binary evolution models for a primary star with $M_{\mathrm{ZAMS}} = 16 M_{\odot}$ (Ouchi & Maeda 2017), the initial orbital period must be $P \sim 800-1200$ days at the formation of the binary system to simultaneously satisfy two conditions: a substantial degree of envelope stripping (reducing the mass of the H-rich envelope to $\lesssim 1 M_{\odot}$) to produce an SN IIb, and a high mass-loss rate in the final ~ 1000 yr. The final mass-loss rate due to binary interaction in such a system is $\sim 10^{-5} M_{\odot}\,\mathrm{yr^{-1}}$, and up to $\sim 6 \times 10^{-5} M_{\odot}\,\mathrm{yr^{-1}}$. While this is lower by a factor of a few than the value estimated for SN 2018ivc (for the outer CSM component), it could at least qualitatively explain the high mass-loss rate. One prediction

from this scenario is that the progenitor had an extended H-rich envelope, as also supported by the optical behavior within the first few days (Section 6.4).

We therefore propose that SN 2018ivc spans the boundary between SNe IIP/IIL and SNe IIb within the binary evolution model. In this interpretation, SN 2018ivc can be regarded as an extreme variant of the SNe IIb showing signatures of a dense CSM (e.g., SN 1993J). Given that this population with a dense CSM, for which binary evolution is a leading scenario, seems to be substantial among SNe IIb (Section 6.1), it seems highly likely that SN 2018ivc also occurred in a binary system. If we assume that typical SNe IIb (including 1993J and 2011dh) and SN 2018ivc–like objects arise from systems with initial orbital periods between 10 and 800 days and between 800 and 1200 days, respectively, we would estimate the rate of SN 2018ivc–like events is $\sim$10% of that of SNe IIb assuming that the distribution of initial orbital periods follows $f(P) \propto P^{-1}$.

To compare this expectation with an observationally inferred rate of SN 2018ivc–like objects, we assume that the number of known events potentially similar to SN 2018ivc (e.g., SN 1996al) would be $\sim$2 or 3. The observed fraction of SNe IIb relative to the whole SESN population in a volume-limited sample, like that of the Lick Observatory Supernova Search (LOSS), is $\sim$25%–35% (Li et al. 2011; Shivvers et al. 2017). Given that the number of relatively well-observed SESNe is $\sim$200 (Ouchi et al. 2021; Fang et al. 2022), the number of well-observed SNe IIb is thus $\sim$50–70. The (very rough) fraction of SN 2018ivc–like events relative to canonical SESNe is therefore $\sim$3%–6%. This estimate roughly matches expectations from the binary evolution scenario proposed here, though we emphasize that this is a very crude estimate and involves large uncertainties both in the model prediction and in the observational numbers.

This scenario predicts that at least a fraction of SNe IIL also originate in binary systems, but this channel for SNe IIL is probably not the major one. As with the above estimate for SN 2018ivc–like events, we can estimate the fraction of SNe IIL undergoing binary interaction by assuming that systems with $P \sim 1200$–2000 days would leave $\lesssim 5 M_\odot$ of the H-rich envelope and potentially become SNe IIL. Relative to SNe IIb this fraction would be $\sim$10%–20%. On the other hand, the observed fractions of SNe IIb and SNe IIL are comparable (Li et al. 2011). This suggests, based on our binary evolution scenario for SN 2018ivc (or more generally on the standard binary evolution scenario toward SNe IIb and SESNe; Ouchi & Maeda 2017), that about 10%–20% of SNe IIL can be intrinsically and directly linked to SESNe in binary systems and can have progenitors with the same ZAMS mass range as that of (canonical) SNe IIP and SESNe; the main difference here is only in the initial binary separation. This could have interesting implications for the origin(s) and population(s) of SNe IIL in that most SNe IIL will require a very different progenitor evolution from that of SNe IIP and SESNe, and their progenitor ZAMS mass ranges may be different. For example, it may well be that single massive stars (more massive than canonical SNe IIP and SESNe) could give rise to the SNe IIP–IIL–IIb sequence (e.g., Heger et al. 2003; Langer 2012). Further investigation of possible progenitor scenarios toward SNe IIL is important if we are to map different progenitors to different types of SNe (e.g., Moriya et al. 2016; Hiramatsu et al. 2021).

6.4. Implications for Optical Emission in the Earliest Phase

In the r band, the initial peak at ~ -17 is followed by a quick decay by $\sim$0.5 mag in $\sim$5 days (Figure 1; Bostroem et al. 2020). This first peak is more evident at shorter wavelengths, which is typical of SNe IIP and IIb. The widely accepted mechanism to create this rapidly evolving early emission is shock-cooling emission following the shock breakout, either from an extended stellar envelope (Bersten et al. 2012, and references therein) or from a compact/dense ("confined") CSM (Morozova et al. 2015; Moriya et al. 2017, and references therein).

We note that the behavior in the first week since the explosion (i.e., a rapid and bright peak, followed by a quick decay) is similar to that observed for infant SNe IIb (Figure 1). For SN IIb 1993J the early emission has been successfully modeled by shock-cooling emission following the breakout from an extended stellar envelope, with little contribution from the energy stored in the shocked (confined) CSM (Nomoto et al. 1993; Woosley et al. 1994; Bersten et al. 2012).

In our interpretation of SN 2018ivc as an SN IIb with an extended envelope similar to SN 1993J, we expect that SN 2018ivc should behave almost identically in the early shock-cooling phase. The CSM density distribution derived here would not have much of an effect on the properties of the cooling-envelope emission; the diffusion time within the CSM is $\lesssim$1 day and the optical depth of the CSM to Thomson scattering drops below 1 within a day (Figure 10). The similarity in the properties of the early optical emission between SNe 1993J and 2018ivc thus lends support to our interpretation.

We note that this judgment on the possible effect of the CSM is based on the structure at $\gtrsim 5 \times 10^{14}$ cm, which is set by our first ALMA observation on day 4. No direct constraint has been placed on the CSM inside this radius, and indeed further constraining the CSM properties there through the early optical emission is highly interesting. The CSM density of SN 2018ivc at $\sim 5 \times 10^{14}$ cm (set by the mass-loss rate $\sim$10 yr before the explosion) is comparable to the density of the "confined" CSM derived for SNe II and SN Ic 2020oi, and suggests that we have already witnessed the beginning of the "final activity" (Section 6.2). We thus would not expect a huge increase in the CSM density toward the innermost region, given that any fluctuation in mass-loss rate in the final decades leading up to the explosion after entry into the "dynamical" stage is probably only of a factor of a few (Maeda et al. 2021). In any case, modeling of the early cooling emission at optical wavelengths will test our scenario for the progenitor of SN 2018ivc, and will potentially provide a hint as to whether the mass-loss rate is variable in the final $\sim$10 yr. We caution also that the discussion in this section is based on the low-extinction case with $E(B - V) \sim 0.5$ mag; further details on the early emission, including the high-extinction case, will be investigated by A. Reguitti et al. (2022, in preparation).

We note that one major difference between SNe 1993J and 2018ivc in the early light curve is the luminosity at the second peak relative to the earliest-phase emission. The second peak in SN 1993J is about as luminous as the first peak, whereas in SN 2018ivc the second peak is considerably fainter (or perhaps hidden by the interaction-powered light curve). Indeed, some "rapid" SNe IIb presented by Ho et al. (2021) show a similar behavior (i.e., without a luminous second peak, thus lacking

^{56}Ni), which might make them intrinsically similar to SN 2018ivc but without strong CSM interaction (Section 6.1).

7. Summary

SN 2018ivc is an unusual SN II. While it is a variant of SNe IIL, its optical light-curve evolution shows a more complicated behavior than that of canonical SNe IIL. A relatively faint, short plateau (∼20 days) is followed by a rapid and linear decay. The main power source for its optical emission has not been previously identified, and therefore the nature of its progenitor has been largely unknown.

In this paper, we have presented the results of our observations of SN 2018ivc at 100 and 250 GHz with ALMA. Despite its location in close proximity to the core of the Seyfert galaxy NGC 1068 (M77), SN 2018ivc is clearly detected thanks to the high angular resolution and high sensitivity provided by ALMA. Our observations started as early as ∼4 days after the explosion, which makes this one of the earliest detections at millimeter wavelengths of any SN. Covering the long-term evolution up to ∼200 days after the explosion, the data allow us to study the nature of the CSM over a range of physical scales, from ∼5 × 10^{14} cm to ∼2 × 10^{16} cm, covering roughly 2 orders of magnitude.

Our inspection of the multiband light curves and the SED evolution indicates the following:

1. Progenitor: The peak radio properties suggest that the progenitor of SN 2018ivc is similar to that of the prototypical SN IIb 1993J, i.e., an explosion of an He star with a small amount of the H-rich envelope still intact at the time of the explosion. Further, we suggest that it had a massive and extended H-rich envelope among the SN IIb class. Due to the small amount of ^{56}Ni, SN 2018ivc might have looked more like the faint and rapidly evolving SN IIb population than like an SN IIL if the dense CSM had been absent. The low ^{56}Ni production may also be linked to its progenitor star mass being as low as $\lesssim 12 M_\odot$.

2. CSM: The CSM around SN 2018ivc is overall denser than that around SN 1993J. Further, the CSM changes in nature at ∼2 × 10^{15} cm. This indicates that the main mechanism driving mass loss changed at ∼30 yr before the explosion (for $v_w \sim 20$ km s^{-1}). This timescale corresponds to the transition between core and shell C burning, which might play an important role in creating the confined CSM inferred for at least a fraction of SNe IIP and SESNe.

In summary, we suggest that the unusual SN II 2018ivc is in fact quite similar to SN IIb 1993J in its intrinsic properties, and the different appearance in their optical emission can mainly be attributed to the differences in their CSM densities, supplemented by the smaller amount of ^{56}Ni produced in SN 2018ivc than in SN 1993J.

We have modeled the ALMA multiband light curves as well as the optical–NIR bolometric light curve and the X-ray flux detected in the early phase. We have shown that these data sets can be explained primarily by the SN–CSM interaction, with the SN ejecta properties of SN 2018ivc being basically identical to those of SN 1993J.

With the properties of the CSM we derived, we have explored the possible progenitor evolution leading up to SN 2018ivc. Our findings and suggestions can be summarized as follows:

1. The final activity in the last 30 yr: The CSM properties below ∼2 × 10^{15} cm match reasonably well those of the "confined" CSM derived previously for SN IIP 2013fs and SN IIb 2013cu. Further, the final mass-loss rate is similar to that derived for SN Ic 2020oi. We may have witnessed the beginning of the final dynamical evolution stage for SN 2018ivc, and the common mass-loss properties in this stage among canonical SNe IIP and Ic and SN 2018ivc perhaps reflect a similar progenitor ZAMS mass range for these objects.

2. Tracing binary interaction in the last 30–200 yr: We suggest that the outer CSM component ($\gtrsim 2 \times 10^{15}$ cm) has been created in the steady evolution stage before entry into the dynamical phase, and can be attributed to mass loss associated with a binary interaction. The CSM density of SN 2018ivc is higher than those of SNe IIb 1993J and 2011dh by a factor of ∼5 and ∼50, respectively, reflecting the diverse CSM densities found for SNe IIb.

3. A population of SNe IIL in the binary scenario: We suggest that SN 2018ivc and a fraction of SNe IIL represent a missing link between SNe IIP and IIb/Ib/Ic in the binary evolution scenario. In this scenario, the SN 2018ivc–like population are intrinsically identical in terms of the nature of their progenitor stars at birth (i.e., the ZAMS mass) with canonical SNe IIP and SNe IIb/Ib/Ic, with the different outcomes mainly reflecting different initial orbital separations.

4. Implications for the bulk of SNe IIL: Under the binary evolution model, the number of objects interpreted as a "direct" link between SNe IIP and SNe IIb/Ib/Ic, i.e., SN 2018ivc–like events as a variant of SNe IIL, is limited to ∼10%–20% (with large uncertainties) of the entire SN IIL population. As a result the nature of the progenitors (e.g., the ZAMS mass) of most SNe IIL may be different from that of canonical SNe IIP and SNe IIb/Ib/Ic.

The present work has highlighted the power of rapid (and long-term) observations of SNe in millimeter wavelengths, particularly with the combination of high sensitivity and high angular resolution afforded by ALMA. Such observations have become possible only recently, not only with the emerging opportunity for time-domain science with ALMA, but also with the rapid development of transient surveys and multiwavelength follow-up programs with various telescopes. Given the diverse observational properties of SNe, and potential links to diverse channels in stellar evolution toward SNe (including those yet to be clarified, e.g., the final dynamical phase), we hope to expand the sample of such comprehensive observations of SNe for both canonical (e.g., Maeda et al. 2021) and unusual (e.g., this work) events.

Appendix

On the Possible Contribution from Secondary Electrons

Given the relatively high CSM density derived for SN 2018ivc, a question remains as to whether the radio emission is substantially contributed by the secondary electrons following the interaction between relativistic/accelerated protons (or ions) and thermal protons, which is omitted in the current work. Assuming that protons are also accelerated at the FS, one measure is the timescale for the proton–proton (p-p) interaction ($t_{\rm pp} \sim (n_{\rm CSM} \sigma_{\rm pp} c)^{-1}$, where $n_{\rm CSM}$ is the number density of the CSM, c is the speed of light, and $\sigma_{\rm pp} \sim 3 \times 10^{-26}$ cm^2 is the cross section for the p-p interaction). Inserting $\rho_{\rm CSM} = 5 \times 10^{11} A_* r^{-2}$ g cm^{-3}, we estimate that $t_{\rm pp} \sim$ 27 days $(A_*/1500)^{-1}(r/10^{15}$ cm$)^2$ for SN 2018ivc. This suggests that the secondary electrons would not produce a major contribution to the synchrotron emission from SN 2018ivc even within the first 10 days.

For comparison, we take the models for SN IIn 2010jl and SN Ib–IIn 2014C from Murase et al. (2019). For SN 2010jl, Murase et al. (2019) adopted $n_{\rm CSM} = 1.8 \times 10^9$ cm^{-3} at $r = 10^{16}$ cm, i.e., $A_* \sim 6 \times 10^5$, for the model on day 300. For SN 2014C, $n_{\rm CSM} = 3.5 \times 10^6$ cm^{-3} at $r = 6.4 \times 10^{16}$ cm, i.e., $A_* \sim 5 \times 10^4$, for the model on day 400. With these values, we estimate that $t_{\rm pp}/t_{\rm hyd} \sim 0.02$ and 8 for SNe 2010jl and 2014C, respectively. Under these conditions, the model emission at ~ 100 GHz computed by Murase et al. (2019) is dominated by the secondary electrons for SN 2010jl and by the primary electrons for SN 2014C. The estimate on $t_{\rm pp}/t_{\rm hyd}$ for SN 2018ivc is similar to the case for SN 2014C, which suggests that the primary electrons (included in our model) provide the major contribution, while the secondary electrons (omitted from our model) can make only a minor contribution. We further note that Murase et al. (2019) assumed $\epsilon_{\rm e} \sim$ a few 10^{-4}, which is an order of magnitude smaller than that in our final model (Model A). For the same CSM density but

adopting the $\epsilon_{\rm e} \sim 0.004$ derived for SN 2018ivc, the contribution of the secondary electrons to the radio emission relative to that of the primary electrons should further decrease. In summary, we conclude that the contribution from the secondary electrons will be negligible for SN 2018ivc, even if it were included in the model calculation. We also note that the contribution from the secondary electrons must be totally negligible in the late phase at $\gtrsim 20$ days.

ORCID iDs

Keiichi Maeda ● https://orcid.org/0000-0003-2611-7269
Poonam Chandra ● https://orcid.org/0000-0002-0844-6563
Takashi J. Moriya ● https://orcid.org/0000-0003-1169-1954
Andrea Reguitti ● https://orcid.org/0000-0003-4254-2724
Stuart Ryder ● https://orcid.org/0000-0003-4501-8100
Tomoki Matsuoka ● https://orcid.org/0000-0002-6916-3559
Tomonari Michiyama ● https://orcid.org/0000-0003-2475-7983
Giuliano Pignata ● https://orcid.org/0000-0003-0006-0188
Daichi Hiramatsu ● https://orcid.org/0000-0002-1125-9187
K. Azalee Bostroem ● https://orcid.org/0000-0002-4924-444X
Esha Kundu ● https://orcid.org/0000-0002-4807-379X
Hanindyo Kuncarayakti ● https://orcid.org/0000-0002-1132-1366
Melina C. Bersten ● https://orcid.org/0000-0002-6991-0550
David Pooley ● https://orcid.org/0000-0003-4897-7833
Shiu-Hang Lee ● https://orcid.org/0000-0002-2899-4241
Daniel Patnaude ● https://orcid.org/0000-0002-7507-8115
Ósmar Rodríguez ● https://orcid.org/0000-0001-8651-8772
Gaston Folatelli ● https://orcid.org/0000-0001-5247-1486

References

Afsariardchi, N., Drout, M. R., Khatami, D. K., et al. 2021, ApJ, 918, 89
Anderson, J. P. 2019, A&A, 628, A7
Anderson, J. P., González-Gaitán, S., Hamuy, M., et al. 2014, ApJ, 786, 67
Anderson, J. P., Habergham, S. M., James, P. A., & Hamuy, M. 2012, MNRAS, 424, 1372
Arcavi, I., Gal-Yam, A., Cenko, S. B., et al. 2012, ApJL, 756, L30
Barbon, R., Ciatti, F., & Rosino, L. 1979, A&A, 72, 287
Benetti, S., Chugai, N. N., Utrobin, V. P., et al. 2016, MNRAS, 456, 3296
Bersten, M. C., Benvenuto, O. G., Nomoto, K., et al. 2012, ApJ, 757, 31
Bersten, M. C., Folatelli, G., García, F., et al. 2018, Natur, 554, 497
Bietenholz, M. F., Bartel, N., Argo, M., et al. 2021, ApJ, 908, 75
Björnsson, C.-I., & Fransson, C. 2004, ApJ, 605, 823
Bostroem, K. A., Valenti, S., Sand, D. J., et al. 2020, ApJ, 895, 31
Bufano, F., Pignata, G., Bersten, M., et al. 2014, MNRAS, 439, 1807
Cardelli, J. A., Clayton, G. C., & Mathis, J. S. 1989, ApJ, 345, 245
Chevalier, R. A. 1982, ApJ, 258, 790
Chevalier, R. A. 1998, ApJ, 499, 810
Chevalier, R. A., & Fransson, C. 2006, ApJ, 651, 381
Chevalier, R. A., & Soderberg, A. M. 2010, ApJL, 711, L40
Chugai, N. N. 2001, MNRAS, 326, 1448
Chugai, N. N. 2009, MNRAS, 400, 866
Davis, S., Pessi, P. J., Fraser, M., et al. 2021, ApJ, 909, 145
Dessart, L., & Hillier, D. J. 2022, A&A, 660, L9
Fang, Q., Maeda, K., Kuncarayakti, H., et al. 2022, ApJ, 928, 151
Fang, Q., Maeda, K., Kuncarayakti, H., Sun, F., & Gal-Yam, A. 2019, NatAs, 3, 434
Filippenko, A. V. 1997, ARA&A, 35, 309
Folatelli, G., Bersten, M. C., Kuncarayakti, H., et al. 2015, ApJ, 811, 147
Fransson, C., & Björnsson, C.-I. 1998, ApJ, 509, 861
Fremling, C., Ko, H., Dugas, A., et al. 2019, ApJL, 878, L5
Fuller, J. 2017, MNRAS, 470, 1642
Gal-Yam, A., Arcavi, I., Ofek, E. O., et al. 2014, Natur, 509, 471
Groh, J. H. 2014, A&A, 572, L11
Groh, J. H., Meynet, G., & Ekström, S. 2013, A&A, 550, L7

Gutiérrez, C. P., Anderson, J. P., Hamuy, M., et al. 2014, ApJL, 786, L15
Heger, A., Fryer, C. L., Woosley, S. E., Langer, N., & Hartmann, D. H. 2003, ApJ, 591, 288
Hiramatsu, D., Howell, D. A., Moriya, T. J., et al. 2021, ApJ, 913, 55
Ho, A. Y. Q., Perley, D. A., Gal-Yam, A., et al. 2021, arXiv:2105.08811
Horesh, A., Sfaradi, I., Ergon, M., et al. 2020, ApJ, 903, 132
Immler, S., & Wang, Q. D. 2001, ApJ, 554, 202
Kasen, D., & Woosley, S. E. 2009, ApJ, 703, 2205
Kilpatrick, C. D., Coulter, D. A., Foley, R. J., et al. 2022, ApJ, 936, 111
Kuncarayakti, H., Anderson, J. P., Galbany, L., et al. 2018, A&A, 613, A35
Langer, N. 2012, ARA&A, 50, 107
Li, W., Leaman, J., Chornock, R., et al. 2011, MNRAS, 412, 1441
Lyman, J. D., Bersier, D., James, P. A., et al. 2016, MNRAS, 457, 328
Maeda, K. 2012, ApJ, 758, 81
Maeda, K. 2013a, ApJ, 762, 14
Maeda, K. 2013b, ApJL, 762, L24
Maeda, K., Chandra, P., Matsuoka, T., et al. 2021, ApJ, 918, 34
Maeda, K., Hattori, T., Milisavljevic, D., et al. 2015, ApJ, 807, 35
Maeda, K., Katsuda, S., Bamba, A., Terada, Y., & Fukazawa, Y. 2014, ApJ, 785, 95
Maeda, K., Mazzali, P. A., Deng, J., et al. 2003, ApJ, 593, 931
Maeda, K., & Moriya, T. J. 2022, ApJ, 927, 25
Margutti, R., Kamble, A., Milisavljevic, D., et al. 2017, ApJ, 835, 140
Margutti, R., Milisavljevic, D., Soderberg, A. M., et al. 2014, ApJ, 780, 21
Martinez, L., Bersten, M. C., Anderson, J. P., et al. 2022, A&A, 660, A41
Matheson, T., Filippenko, A. V., Ho, L. C., Barth, A. J., & Leonard, D. C. 2000a, AJ, 120, 1499
Matheson, T., Filippenko, A. V., Barth, A. J., et al. 2000b, AJ, 120, 1487
Matsuoka, T., Maeda, K., Lee, S.-H., & Yasuda, H. 2019, ApJ, 885, 41
Maund, J. R., Fraser, M., Ergon, M., et al. 2011, ApJL, 739, L37
Maund, J. R., Smartt, S. J., Kudritzki, R. P., Podsiadlowski, P., & Gilmore, G. F. 2004, Natur, 427, 129
Meza, N., & Anderson, J. P. 2020, A&A, 641, A177
Moriya, T. J., Pruzhinskaya, M. V., Ergon, M., & Blinnikov, S. I. 2016, MNRAS, 455, 423
Moriya, T. J., Yoon, S.-C., Gräfener, G., & Blinnikov, S. I. 2017, MNRAS Lett., 469, L108
Morozova, V., Piro, A. L., Fuller, J., & Van Dyk, S. D. 2020, ApJL, 891, L32
Morozova, V., Piro, A. L., Renzo, M., et al. 2015, ApJ, 814, 63

Morozova, V., Piro, A. L., & Valenti, S. 2017, ApJ, 838, 28
Murase, K., Franckowiak, A., Maeda, K., Margutti, R., & Beacom, J. F. 2019, ApJ, 874, 80
Nakaoka, T., Moriya, T. J., Tanaka, M., et al. 2019, ApJ, 875, 76
Nomoto, K., Suzuki, T., Shigeyama, T., et al. 1993, Natur, 364, 507
Ouchi, R., & Maeda, K. 2017, ApJ, 840, 90
Ouchi, R., Maeda, K., Anderson, J. P., & Sawada, R. 2021, ApJ, 922, 141
Pastorello, A., Smartt, S. J., Mattila, S., et al. 2007, Natur, 447, 829
Pessi, P. J., Folatelli, G., Anderson, J. P., et al. 2019, MNRAS, 488, 4239
Popov, D. V. 1993, ApJ, 414, 712
Quataert, E., & Shiode, J. 2012, MNRAS Lett., 423, L92
Richmond, M. W., Treffers, R. R., Filippenko, A. V., et al. 1994, AJ, 107, 1022
Rodríguez, Ó., Meza, N., Pineda-García, J., & Ramirez, M. 2021, MNRAS, 505, 1742
Shigeyama, T., Suzuki, T., Kumagai, S., et al. 1994, ApJ, 420, 341
Shivvers, I., Modjaz, M., Zheng, W., et al. 2017, PASP, 129, 054201
Smartt, S. J. 2009, ARA&A, 47, 63
Smartt, S. J. 2015, PASA, 32, e016
Soderberg, A. M., Margutti, R., Zauderer, B. A., et al. 2012, ApJ, 752, 78
Sun, N.-C., Maund, J. R., & Crowther, P. A. 2022, arXiv:2209.05283
Taddia, F., Stritzinger, M. D., Bersten, M., et al. 2018, A&A, 609, A136
Takei, Y., Tsuna, D., Kuriyama, N., Ko, T., & Shigeyama, T. 2022, ApJ, 929, 177
Tartaglia, L., Fraser, M., Sand, D. J., et al. 2017, ApJL, 836, L12
Tartaglia, L., Sand, D. J., Valenti, S., et al. 2018, ApJ, 853, 62
Tully, R. B., Rizzi, L., Shaya, E. J., et al. 2009, AJ, 138, 323
Valenti, S., Sand, D., Stritzinger, M., et al. 2015, MNRAS, 448, 2608
Valenti, S., Sand, D. J., & Wyatt, S. 2018, Transient Name Server Discovery Report, 2018-1816, 1
van Dyk, S. D., Weiler, K. W., Sramek, R. A., Rupen, M. P., & Panagia, N. 1994, ApJL, 432, L115
Van Dyk, S. D., Zheng, W., Fox, O. D., et al. 2014, AJ, 147, 37
Woosley, S. E., Eastman, R. G., Weaver, T. A., & Pinto, P. A. 1994, ApJ, 429, 300
Yamanaka, M. 2018, Transient Name Server Classification Report, 2018-1818, 1
Yaron, O., Perley, D. A., Gal-Yam, A., et al. 2017, NatPh, 13, 510
Yoon, S.-C. 2017, MNRAS, 470, 3970
Zhang, X., Zhang, J., Wang, X., et al. 2018, ATel, 12240, 1